A Technique for Diagnosing Three-Dimensional Ageostrophic Circulations in Baroclinic Disturbances on Limited-Area Domains

ANDREW F. LOUGHE*

Department of Atmospheric Science, State University of New York at Albany, Albany, New York

CHUNG-CHIENG LAI

Earth and Environmental Science Division, Los Alamos National Laboratory, Los Alamos, New Mexico

DANIEL KEYSER

Department of Atmospheric Science, State University of New York at Albany, Albany, New York

(Manuscript received 8 June 1994, in final form 29 September 1994)

ABSTRACT

The methodology developed by Keyser et al. for representing and diagnosing three-dimensional vertical circulations in baroclinic disturbances using a two-dimensional vector streamfunction, referred to as the psi vector, is restricted to *f*-plane channel-model geometry. The vertical circulation described by the psi vector consists of the irrotational (or divergent) part of the ageostrophic wind and the vertical velocity. A key property of the psi vector is that its projections onto arbitrarily oriented orthogonal vertical planes yield independent vertical circulations, allowing separation of a three-dimensional vertical circulation into *two* two-dimensional components, and thus objective assessment of the extent to which a three-dimensional vertical circulation is oriented in a preferred direction. Here the methodology for determining the psi vector is modified to be suitable for real-data applications. The modifications consist of reformulating the diagnostic equations to apply to conformal map projections and to limited-area domains; despite the desirability of incorporating topography, this task is deferred to future research. The geostrophic wind is defined in terms of constant Coriolis parameter, rendering it nondivergent and thus confining the horizontal divergence to the ageostrophic wind. The ageostrophic wind is partitioned into harmonic, rotational, and divergent components. This three-way partition provides a consistency check of the divergent ageostrophic wind recovered from the horizontal divergence field with its counterpart determined from the psi-vector calculation.

The modified psi-vector methodology is illustrated for two well-documented East Coast midlatitude cyclones. The first case (the Presidents' Day storm: 1200 UTC 19 February 1979) considers an interpretation that ascent in the vicinity of a curved upper-level jet–front system may be viewed as a superposition of contributions from cross-stream divergent ageostrophic flow associated with a jet streak and from alongstream divergent ageostrophic flow associated with a baroclinic wave. The second case (the Megalopolitan storm: 1200 UTC 11 February 1983) addresses the hypothesis of Uccellini and Kocin that vertical circulations transverse to meridionally displaced upper-tropospheric jet streaks are coupled in a lateral sense. In both of these cases, the diagnoses reveal that the cross-stream component of the divergent ageostrophic circulation isolates meaningful mesoscale signatures coinciding with regions of precipitation and ascent in the vicinity of upper-level jet–front systems, whereas the alongstream component is indicative of synoptic-scale vertical motion. Furthermore, it is found that the cross-contour ageostrophic flow, necessary for Lagrangian rates of change of kinetic energy in jet entrance and exit regions, is due primarily to the nondivergent (i.e., harmonic plus rotational) ageostrophic wind. This result suggests that the practice of linking cross-contour ageostrophic winds and vertical motions in jet entrance and exit regions in the qualitative assessment of energy transformations in these regions may be problematic in the case of upper-level jet–front systems situated in three-dimensional flows.

1. Introduction

In an earlier paper, Keyser et al. (1989, hereafter referred to as KSD) defined the three-dimensional *vertical circulation* in baroclinic disturbances on an *f* plane as the irrotational[1] part of the ageostrophic wind $\mathbf{V}_{agir}$ and the vertical velocity (ω, in pressure coordi-

* Current affiliation: Cooperative Institute for Research in the Environmental Sciences, University of Colorado, Boulder, CO.

Corresponding author address: Dr. Daniel Keyser, Department of Atmospheric Science, ES-224, State University of New York at Albany, Albany, NY 12222.

[1] Here we use the term "irrotational" in the context of the conventional Helmholtz partition of a two-dimensional vector field (e.g., Dutton 1986, section 5.6.2), where such a vector field is decomposed into irrotational and nondivergent parts. We reserve the use of the terms "divergent" and "rotational" until later in the paper (section 2b), where consideration of lateral boundary conditions on limited-area domains necessitates introducing the harmonic part of the ageostrophic wind.

nates), which are linked kinematically through mass continuity. The vertical circulation may be represented in terms of a two-dimensional vector streamfunction, referred to by KSD as the psi vector. Deferring specification of the horizontal coordinate system until section 2, we define the psi vector generically as

$$\mathbf{V}_{\text{agir}} = -\frac{\partial \boldsymbol{\psi}}{\partial p}, \quad \omega = \nabla_p \cdot \boldsymbol{\psi}. \tag{1.1}$$

In addition to considering the irrotational part of the ageostrophic flow as providing the horizontal branches of three-dimensional vertical circulations, KSD included the nondivergent part in their diagnosis. Accordingly, the combination of the total ageostrophic wind and the vertical velocity will be referred to as the *ageostrophic circulation* in order to be distinguished from the vertical circulation defined above. Although kinematically independent of the vertical velocity, the nondivergent part of the ageostrophic wind was shown in KSD to contribute significantly to the along-contour ageostrophic wind in regions of curved flow and to the cross-contour ageostrophic wind in the entrance and exit regions of jet streaks. The latter result, consistent with the findings of Krishnamurti (1968) and Blackburn (1985),[2] led to the suggestion that, to the extent the cross-contour flow is dominated by the nondivergent part of the ageostrophic wind, vertical motions (and transverse vertical circulations) in jet entrance and exit regions are decoupled from Lagrangian rates of change of kinetic energy. An implication of this suggestion is that caution should be exercised in interpreting and applying observationally derived conceptual models that relate vertical motions in jet entrance and exit regions to the cross-contour component of the total ageostrophic wind. Finally, it should be emphasized that the methodology developed and applied by KSD is kinematic; that is, there is no consideration of the dynamical relationship of the ageostrophic circulation to the mass field. Various alternative formulations relating the ageostrophic circulation to the geostrophic flow based on the quasigeostrophic (QG) equations are presented by Keyser et al. (1992a), Xu (1992), Xu and Keyser (1993), and Keyser (1994).

The representation in (1.1) was adopted with the eventual goal of isolating vertical circulations associated with fronts and jet streaks (to be referred to as jet–front systems) found within realistic three-dimensional flows. Specifically, the cross-front (virtually synonymous with "cross-jet" or "cross-stream") component of the vertical circulation may be extracted by projecting the psi vector onto the plane normal to the long axis of a jet–front system. The relative contributions of the cross- and alongfront components of the three-dimensional vertical circulation may be evaluated by comparing the magnitudes of the vertical motion fields associated with these respective component circulations. (The former dominates the latter in the two-dimensional limit of increasingly anisotropic vertical motion patterns in which the long axis is oriented in the alongfront direction.) Whether or not the cross-front vertical circulation dominates its alongfront counterpart, the cross-front circulation may be compared with signatures derived from idealized dynamical models of frontogenesis. In such comparisons, it should be recognized that in idealized diagnostic and prognostic dynamical models of frontogenesis [see, e.g., reviews by Hoskins (1982) and Eliassen (1990)] the vertical circulation is two-dimensional and confined to the cross-front vertical plane. In such models, the vertical circulation consists of the perturbation (as opposed to basic-state) ageostrophic wind in the cross-front plane and the total vertical motion field, which are linked through mass continuity. The cross-front ageostrophic wind is purely irrotational; this property is extended to three dimensions in the definition of the vertical circulation given by (1.1).

Although the use of a vector–streamfunction representation is not restricted to the irrotational part of the ageostrophic wind [e.g., applications by Hoskins and Draghici (1977) and by Sanders and Bosart (1985) use the total ageostrophic wind and the total horizontal wind, respectively], the present approach exhibits the following desirable attributes (KSD): (i) internal cancellation between the partitioned components of the vertical motion is eliminated; (ii) the vertically integrated mass fluxes of the component vertical circulations in orthogonal vertical planes vanish (i.e., streamlines do not begin or end at boundaries). It may be shown that both of these attributes are a consequence of defining the psi vector in terms of the irrotational part of the ageostrophic wind, coupled with the assumption of vanishing total vertical motion at the bottom and top boundaries, consisting of isobaric surfaces. The former attribute ensures that unrealistically large vertical motions of nearly equal magnitude and of opposite sign do not arise within the component circulations in response to contraction in one direction counterbalancing stretching in the orthogonal direction, as would occur in the presence of a nondivergent wind component. The latter attribute replicates the property that vertical circulations in two-dimensional frontogenesis models are composed of closed cells.

Despite the formulation of the psi-vector methodology to achieve the goal of isolating vertical circulations associated with jet–front systems found within realistic three-dimensional flows, its application in KSD is limited to simulations conducted with an adiabatic, f-plane, primitive equation channel model. In the present paper, we modify the methodology for determining the psi

[2] Blackburn (1985) is concerned with planetary-scale, time-averaged jet streams rather than mesoscale jet streaks associated with transient baroclinic disturbances, the latter of which are the focus of the present paper.

vector to be suitable for real-data applications. The modifications comprise reformulating the diagnostic equations presented in section 2b of KSD for application to conformal map projections and to limited-area domains; these modifications are the subject of section 2 of the present paper. Datasets and computational procedures are described in section 3, while illustrative applications with real data are presented in section 4; the datasets consist of three-dimensional gridded fields for the Presidents' Day storm of February 1979 and for the Megalopolitan storm of February 1983. A summary of the main findings of this study, along with possible extensions, is presented in section 5.

2. Diagnosis of ageostrophic circulations on limited-area domains

In this section, we adapt the kinematic methodology of KSD for representing and diagnosing ageostrophic circulations for application to limited-area domains. Toward this end, we consider a Cartesian grid on a conformal map projection; for details concerning conformal map projections, such as definition of grids, expressions for map-scale factors, and the form of the primitive equations, the interested reader is referred to Saucier (1955, sections 2.11–2.15), Haltiner and Williams (1980, section 1.8), Anthes et al. (1987, appendix 4), and Danard (1989). Next, we define the geostrophic wind in terms of constant Coriolis parameter, rendering it nondivergent. Following this step, we apply the three-component partition of a two-dimensional vector field described by Lynch (1989, section 3) to the ageostrophic wind. The divergent part of the ageostrophic wind included in this partition corresponds to that derived from the psi vector (1.1), the latter of which is determined from the vertical motion field. Finally, we conclude with expressions applicable to a conformal map projection for the QG omega equation, equivalent potential vorticity, and absolute vector vorticity, each of which will be used in the interpretation of the vertical circulation patterns in section 4.

a. Definition of geostrophic wind and mass continuity

One may define the geostrophic wind in pressure coordinates on a conformal grid as

$$f_0\mathbf{V}_g = \mathbf{k} \times m\nabla_p\phi, \tag{2.1}$$

where f_0 is a constant value of the Coriolis parameter, taken to be the value of f at the center of the domain; m is the map-scale factor; $\nabla_p \equiv \mathbf{i}\partial/\partial x_p + \mathbf{j}\partial/\partial y_p$ is the horizontal gradient operator on a pressure surface; ϕ ($=gh$) is geopotential; and x and y refer to distances in the $\mathbf{i}$ and $\mathbf{j}$ directions with respect to the map projection. The geostrophic wind as defined in (2.1) is nondivergent, so that the continuity equation in pressure coordinates may be written

$$m^2\nabla_p \cdot \left(\frac{\mathbf{V}_{ag}}{m}\right) = -\frac{\partial\omega}{\partial p}. \tag{2.2}$$

It should be recognized that the constant-f definition of the geostrophic wind (2.1) does not change the pressure gradient force, which is invariant in the vector momentum equation. Nevertheless, this definition does change the interpretation of the vector momentum equation for frictionless flow; this equation now may be written as

$$\frac{d\mathbf{V}}{dt} = -f_0\mathbf{k} \times \mathbf{V}_{ag} - (f - f_0)(\mathbf{k} \times \mathbf{V}), \tag{2.3}$$

where $\mathbf{V} = u\mathbf{i} + v\mathbf{j}$, such that $mu = dx/dt$ and $mv = dy/dt$, and

$$\frac{d\mathbf{V}}{dt} = \frac{\partial\mathbf{V}}{\partial t} + m(\mathbf{V}\cdot\nabla_p)\mathbf{V} + \left(u\frac{\partial m}{\partial y} - v\frac{\partial m}{\partial x}\right)(\mathbf{k} \times \mathbf{V}) + \omega\frac{\partial\mathbf{V}}{\partial p}. \tag{2.4}$$

Inspection of (2.3) reveals that the vector momentum equation based on (2.1) possesses not only the conventional Coriolis term, but also a second term accounting for the variation of f relative to its central value. Because the acceleration represented by this additional term is oriented normal to the wind velocity, it only modifies the wind direction. Consequently, Lagrangian rates of change of kinetic energy are due only to the cross-contour component of the ageostrophic wind, as is the case where the geostrophic wind is defined in terms of variable f. Further discussion and comparison of the properties of constant- and variable-f definitions of the geostrophic wind may be found in Blackburn (1985).

b. Three-component partition of the ageostrophic wind

The following discussion assumes that the ageostrophic wind is known a priori and that it is to be partitioned for diagnostic purposes. This situation corresponds to the "partitioning problem" as defined by Bijlsma et al. (1986). The partitioning problem should be distinguished from the related "reconstruction problem," which concerns recovering the wind field from the vertical component of the relative vorticity and the horizontal divergence, which in the case of a limited-area domain requires knowledge of the wind velocity on the domain boundaries. Both problems, which are especially relevant to diagnostic studies and to initialization of numerical prediction models, have been treated comprehensively in recent years by Bijlsma et al. (1986), Lynch (1988, 1989), and Chen and Kuo (1992a,b); the interested reader is directed to these references for background material. In the remainder of this subsection, we adapt the three-component partition

described by Lynch (1989, section 3) to the ageostrophic wind field.

We decompose the ageostrophic wind based on the constant-f definition of the geostrophic wind into harmonic, rotational, and divergent parts:

$$\mathbf{V}_{ag} = \mathbf{V}_{agh} + \mathbf{V}_{agr} + \mathbf{V}_{agd}. \tag{2.5}$$

The harmonic part of the ageostrophic wind may be defined either in terms of a velocity potential Φ_h or a streamfunction Ψ_h:

$$\mathbf{V}_{agh} = m\nabla_p\Phi_h = \mathbf{k} \times m\nabla_p\Psi_h, \tag{2.6}$$

satisfying

$$\nabla_p^2\Phi_h = 0 \quad \text{and} \quad \nabla_p^2\Psi_h = 0 \tag{2.7}$$

and subject to suitable nonhomogeneous lateral boundary conditions, to be discussed subsequently. The rotational and divergent parts of the ageostrophic wind are defined in terms of a streamfunction Ψ_r and velocity potential Φ_d, respectively:

$$\mathbf{V}_{agr} = \mathbf{k} \times m\nabla_p\Psi_r, \tag{2.8}$$

$$\mathbf{V}_{agd} = m\nabla_p\Phi_d, \tag{2.9}$$

such that

$$m^2\nabla_p^2\Psi_r = \zeta_{ag}, \tag{2.10}$$

and

$$m^2\nabla_p^2\Phi_d = \delta_{ag}, \tag{2.11}$$

subject to homogeneous Dirichlet conditions on Ψ_r and Φ_d on the lateral boundaries. In (2.10) and (2.11), ζ_{ag} and δ_{ag} are the vertical component of relative vorticity and the horizontal divergence of the ageostrophic wind, respectively:

$$\zeta_{ag} = m^2\mathbf{k}\cdot\nabla_p \times \left(\frac{\mathbf{V}_{ag}}{m}\right), \tag{2.12}$$

and δ_{ag} are given by the left-hand side of (2.2).

The presence of the harmonic part of the ageostrophic wind, which is both nondivergent and irrotational, in the decomposition (2.5) leads to the adoption of the terms "rotational" and "divergent" to describe the parts of the ageostrophic wind associated with the ageostrophic vorticity and divergence fields, respectively. The following relationships apply (Xu and Keyser 1993):

$$\mathbf{V}_{agir} = \mathbf{V}_{agh} + \mathbf{V}_{agd}, \tag{2.13a}$$

$$\mathbf{V}_{agnd} = \mathbf{V}_{agh} + \mathbf{V}_{agr}. \tag{2.13b}$$

Use of (2.13a) and (2.13b) in conjunction with (2.5) yields

$$\begin{aligned}\mathbf{V}_{ag} &= \mathbf{V}_{agnd} + \mathbf{V}_{agd} \\ &= \mathbf{V}_{agir} + \mathbf{V}_{agr} = \mathbf{V}_{agnd} + \mathbf{V}_{agir} - \mathbf{V}_{agh}.\end{aligned} \tag{2.14}$$

Despite the labels "rotational" and "divergent," these respective parts of the ageostrophic wind still possess kinematic properties other than vorticity and divergence (e.g., deformation and translation). In the case of a disturbance that is sufficiently localized on a limited-area domain and in the cases of global or doubly periodic domains, the harmonic part of the ageostrophic wind vanishes, and there is no distinction between "irrotational" and "divergent" (2.13a) and between "nondivergent" and "rotational" (2.13b). In such cases, the former, exclusive terminology may be preferable because it offers a reminder that the irrotational and nondivergent parts of the wind account for all kinematic properties except vorticity and divergence, respectively.

Lynch (1989) shows that the harmonic velocity potential Φ_h and harmonic streamfunction Ψ_h form two sets of isopleths orthogonal to each other everywhere on a limited-area domain. This property is a straightforward consequence of (2.6) [i.e., $\mathbf{V}_{agh}\cdot(\mathbf{k} \times \mathbf{V}_{agh}) = 0$, where the first $\mathbf{V}_{agh}$ is defined in terms of Φ_h and the second in terms of Ψ_h]. Specification of lateral boundary conditions for Φ_h and Ψ_h is possible given either the tangential (v_{ags}) or normal (v_{agn}) ageostrophic velocity components (where, in this context, the positive s and n directions are counterclockwise and outward with respect to the domain boundary); it is not necessary to use both components simultaneously. If v_{ags} (v_{agn}) is used, then Dirichlet conditions result for Φ_h (Ψ_h) and Neumann conditions for Ψ_h (Φ_h). In the present paper, we restrict consideration to v_{ags}, adopting Dirichlet conditions (on Φ_h) for all calculations to be shown involving the harmonic ageostrophic wind, because different staggered grids are required for v_{ags} and v_{agn} (Lynch 1989, p. 1495). Calculations with Neumann conditions (on Ψ_h) were performed as a consistency check of their Dirichlet counterparts. The preference for presenting results based on the Dirichlet option is dictated by more rapid convergence using successive overrelaxation in solving (2.7) numerically.

Expressions for Φ_h and Ψ_h on the lateral boundaries are given as follows:

$$\Phi_h(s) = \int_0^s \left(v_{ags} - m\frac{\partial\Psi_r}{\partial n}\right)\frac{ds}{m}, \tag{2.15}$$

and

$$\frac{\partial\Psi_h}{\partial n} = \frac{v_{ags}}{m} - \frac{\partial\Psi_r}{\partial n}. \tag{2.16}$$

These expressions are derived from the equation relating v_{ags} to Ψ and Φ on the lateral boundaries (i.e., $v_{ags} = m\partial\Psi/\partial n + m\partial\Phi/\partial s$, with $\Psi = \Psi_h + \Psi_r$ and $\Phi = \Phi_h + \Phi_d\Delta_d$). Noting that $\partial\Phi_d/\partial s = 0$ on the lateral boundaries, and assuming that $\Psi_h = 0$ ($\Phi_h = 0$) on the lateral boundaries and thus vanishes everywhere within the domain interior according to (2.7), we obtain (2.15) [(2.16)]. Equations (2.15) and (2.16) corre-

spond to alternatives 7 and 5, respectively, of Lynch (1989), which are variations on a method credited originally to Sangster (1960).

The decomposition of the ageostrophic wind (2.5), such that the rotational and divergent parts are determined subject to homogeneous Dirichlet conditions on streamfunction and velocity potential, has the properties that the domain-averaged kinetic energy of the rotational and divergent parts of the ageostrophic wind is minimized and that each part of the ageostrophic wind in (2.5) is orthogonal in a domain-averaged sense to the other two (e.g., Lynch 1989). The latter property is attractive because it eliminates the possibility of cross terms, which are free to assume nonphysical negative values, in the expression for domain-averaged kinetic energy. It should be recognized that the alternative of homogeneous Dirichlet boundary conditions on streamfunction and velocity potential renders the decomposition in (2.5) domain dependent in the following sense: the rotational and divergent (and thus harmonic) winds associated with vorticity and divergence features localized in the domain interior are a function of the proximity of the domain boundaries to these features and of the geometry (shape) of the boundaries.

Very recently, Bishop (1995) has proposed and demonstrated the use of free-space Green's functions to attribute the rotational and divergent parts of a wind field to localized vorticity and divergence features in a domain-independent manner. In this approach, the harmonic wind is the residual between the total wind and the sum of the divergent and rotational parts of the wind, consistent with (2.5), and the harmonic wind arises from divergence and vorticity features outside of the domain (Chen and Kuo 1992a, section 3c; Bishop 1995). Nevertheless, it should be recognized that in Bishop's approach the kinetic energy of the rotational and divergent components is no longer minimized and that the partitioned wind components are no longer pairwise orthogonal, because Φ_d and Ψ_r do not vanish in general on the boundaries. Moreover, for domains in which discrete vorticity and divergence features cannot be identified readily, as is typically the case with observed datasets, the relative contributions of the divergent, rotational, and harmonic parts of the wind to the total wind at any point in the domain will be a function of the location and geometry of the lateral boundaries. Thus, it appears that achieving a truly domain-independent decomposition of horizontal wind fields into divergent and rotational parts requires consideration of global geometry.

c. *Computation of vertical motion and diagnosis of the psi vector*

In the context of the three-component partition of the ageostrophic wind (2.5), we rewrite (1.1) as

$$\mathbf{V}_{agd} = -\frac{\partial \boldsymbol{\psi}}{\partial p}, \quad \omega = m^2 \nabla_p \cdot \left(\frac{\boldsymbol{\psi}}{m}\right). \tag{2.17}$$

The psi vector may be calculated from the vertical motion according to the relationship

$$\omega = -m^2 \nabla_p^2 \chi, \tag{2.18}$$

where

$$\boldsymbol{\psi} = -m \nabla_p \chi \tag{2.19a}$$

and

$$\mathbf{V}_{agd} = m \nabla_p \frac{\partial \chi}{\partial p}. \tag{2.19b}$$

Substituting (2.18) and (2.19b) into (2.2), and recalling from (2.14) that $\mathbf{V}_{ag} = \mathbf{V}_{agnd} + \mathbf{V}_{agd}$, confirms that the definition of the psi vector (2.17) satisfies mass continuity. In subsequent diagnoses of $\boldsymbol{\psi}$, we solve (2.18) for χ, assuming homogeneous Dirichlet conditions on the lateral boundaries, and then diagnose $\boldsymbol{\psi}$ from χ (2.19a). Comparison of (2.9) and (2.19b) reveals that $\Phi_d = \partial\chi/\partial p$, so assuming that χ equals zero on the lateral boundaries is consistent with specifying homogeneous Dirichlet conditions on Φ_d. The compatibility between the lateral boundary conditions on χ and Φ_d provides a consistency check of $\mathbf{V}_{agd}$ calculated from $\boldsymbol{\psi}$ using (2.17) [or (2.19b)] with its counterpart calculated from Φ_d (2.9). Such a consistency check, to be discussed in section 3, makes use of (2.17).

The psi-vector components are then used to determine the projections of the divergent ageostrophic circulation onto orthogonal vertical planes, to be referred to as the cross- and alongfront (or cross- and along-jet) planes. For this purpose, we adopt a right-handed Cartesian coordinate system (s, n), oriented such that s and n denote the cross- and alongfront directions. The resulting projections are

$$v_{agds} = -\frac{\partial \psi_s}{\partial p},$$

$$\omega_s = m^2 \frac{\partial}{\partial s}\left(\frac{\psi_s}{m}\right) \quad (s, p) \text{ plane}, \tag{2.20a}$$

$$v_{agdn} = -\frac{\partial \psi_n}{\partial p},$$

$$\omega_n = m^2 \frac{\partial}{\partial n}\left(\frac{\psi_n}{m}\right) \quad (n, p) \text{ plane}. \tag{2.20b}$$

Inspection of (2.20a) and (2.20b) shows that (v_{agds}, ω_s) and (v_{agdn}, ω_n) satisfy continuity individually in the (s, p) and (n, p) planes.

Projecting $\boldsymbol{\psi}$ onto the cross- and alongfront planes is achieved computationally by rotating the x and y components of $\boldsymbol{\psi}$ into the s and n directions:

$$\psi_s = \psi_x \cos\alpha + \psi_y \sin\alpha, \tag{2.21a}$$

$$\psi_n = -\psi_x \sin\alpha + \psi_y \cos\alpha, \tag{2.21b}$$

where α is the rotation angle from the positive x axis (counterclockwise positive). The quantities ω_s and ω_n [(2.20a) and (2.20b)] are evaluated from the corresponding expressions in the (x, y) coordinate system. Partial derivatives with respect to s and n transform as follows:

$$\frac{\partial}{\partial s} = \cos\alpha\left(\frac{\partial}{\partial x}\right) + \sin\alpha\left(\frac{\partial}{\partial y}\right), \quad (2.22a)$$

$$\frac{\partial}{\partial n} = -\sin\alpha\left(\frac{\partial}{\partial x}\right) + \cos\alpha\left(\frac{\partial}{\partial y}\right). \quad (2.22b)$$

Use of (2.21a) and (2.22a) in conjunction with (2.20a) leads to the desired expression for ω_s; an analogous procedure yields ω_n:

$$\omega_s = m^2\left\{\cos^2\alpha\,\frac{\partial}{\partial x}\left(\frac{\psi_x}{m}\right) + \left[\frac{\partial}{\partial x}\left(\frac{\psi_y}{m}\right) + \frac{\partial}{\partial y}\left(\frac{\psi_x}{m}\right)\right] \times \sin\alpha\cos\alpha + \sin^2\alpha\,\frac{\partial}{\partial y}\left(\frac{\psi_y}{m}\right)\right\}, \quad (2.23a)$$

$$\omega_n = m^2\left\{\sin^2\alpha\,\frac{\partial}{\partial x}\left(\frac{\psi_x}{m}\right) - \left[\frac{\partial}{\partial x}\left(\frac{\psi_y}{m}\right) + \frac{\partial}{\partial y}\left(\frac{\psi_x}{m}\right)\right] \times \sin\alpha\cos\alpha + \cos^2\alpha\,\frac{\partial}{\partial y}\left(\frac{\psi_y}{m}\right)\right\}. \quad (2.23b)$$

The sum of (2.23a) and (2.23b) reduces to the second member of (2.17), consistent with the invariance of the horizontal divergence operator with respect to a rotation of coordinate axes.

d. Additional diagnostics

The Q-vector form of the adiabatic, frictionless QG omega equation (e.g., Hoskins et al. 1978; Hoskins and Pedder 1980; Holton 1992, section 6.4.2) is solved in order to provide a qualitative consistency check of the kinematic vertical motion. An approximate form of this equation incorporating map scale factors is given by

$$\sigma m^2\nabla_p^2\omega + f_0^2\frac{\partial^2\omega}{\partial p^2} = -2hm^2\nabla_p\cdot\left(\frac{\mathbf{Q}}{m}\right), \quad (2.24)$$

where

$$\mathbf{Q} = -m^2\left(\frac{\partial\mathbf{V}_g}{\partial x}\cdot\nabla_p\theta\right)\mathbf{i} - m^2\left(\frac{\partial\mathbf{V}_g}{\partial y}\cdot\nabla_p\theta\right)\mathbf{j}. \quad (2.25)$$

In (2.24), h [$=(\rho\theta)^{-1}$] is a pressure-dependent function that may be expressed equivalently as $h = (R/p_0)(p_0/p)^{c_v/c_p}$, where p_0 is a reference pressure (1000 mb). [Note that h in (2.24) should be distinguished from its usage later to denote geopotential height (ϕ/g).] The static stability coefficient is given by $\sigma = -hd\Theta/dp$, where Θ is the average potential temperature on a given pressure level. Neglected in (2.24) and (2.25) are terms representing the variation of the Coriolis parameter on the conformal grid ("β" terms) and small terms involving horizontal gradients of map-scale factors.

In order to assess the stability of the flow to slantwise parcel displacements, we calculate the equivalent potential vorticity PV_e. Selection of this diagnostic is motivated by the theory of conditional symmetric instability (e.g., Bennetts and Hoskins 1979; Emanuel 1983a,b; Knight and Hobbs 1988, section 3; Emanuel 1994, chapter 12), although it is recognized that this theory is applicable strictly to two-dimensional flows (no variations in the alongfront direction). The equivalent potential vorticity in pressure coordinates is

$$\mathrm{PV}_e = -g(\zeta_p + f)\frac{\partial\theta_e}{\partial p} + gm\left(\frac{\partial v}{\partial p}\frac{\partial\theta_e}{\partial x} - \frac{\partial u}{\partial p}\frac{\partial\theta_e}{\partial y}\right), \quad (2.26)$$

where ζ_p is the vertical component of relative vorticity of the total wind in pressure coordinates [refer to (2.12) for the form of this quantity on a conformal map projection] and f is a local value of the Coriolis parameter. The equivalent potential temperature θ_e is calculated following Bolton (1980).

The expression for PV_e (2.26) is equivalent to $g\boldsymbol{\zeta}_a\cdot(m\nabla_p\theta_e - \mathbf{k}\partial\theta_e/\partial p)$, where

$$\boldsymbol{\zeta}_a = \left(\frac{\partial v}{\partial p}\right)\mathbf{i} - \left(\frac{\partial u}{\partial p}\right)\mathbf{j} + (\zeta_p + f)\mathbf{k} \quad (2.27)$$

is the absolute vector vorticity. In order to provide a two-dimensional visualization of the PV_e field, we plot the vector component of (2.27) in the (s, p) plane, $(\partial v_n/\partial p)\mathbf{s} + (\zeta_p + f)\mathbf{k}$, and superimpose it upon a background of θ_e. This display is motivated by considering the special case of two-dimensional flow ($\partial/\partial n = 0$); in this case the sign and relative magnitude of PV_e may be assessed visually from the relative orientation of vectors defined by $(\partial v_n/\partial p)\mathbf{s} + (\partial v_n/\partial s + f)\mathbf{k}$ and contours of constant θ_e. Of interest in the subsequent diagnostic analyses will be to identify regions of vanishing conditional symmetric stability ($\mathrm{PV}_e = 0$). These regions are hypothesized to indicate the recent or concomitant occurrence of slantwise moist convection (e.g., Emanuel 1994, section 12.3), yielding an environment particularly conducive to forced slantwise ascent. In the two-dimensional limit, the vanishing of PV_e corresponds to the coincidence of the two-dimensional absolute vorticity vectors and contours of constant θ_e on the (s, p) plane.

3. Datasets and computational procedures

Diagnostic analyses of the three-dimensional ageostrophic circulations to be considered in this and the following section are based on gridded datasets for the

Presidents' Day storm at 1200 UTC 19 February 1979 (to be referred to as the "PD case") and for the Megalopolitan storm at 1200 UTC 11 February 1983 (to be referred to as the "M case"). The gridded dataset for the PD case is that prepared for a diagnostic study of this storm by Bosart and Lin (1984). Their dataset was developed through subjective modification of the National Meteorological Center (NMC) analysis of geopotential height h, temperature T, relative humidity RH, and total wind $\mathbf{V}$ on a 2.5° latitude–longitude grid. The resulting analyses reside on a 1° latitude–longitude grid on 10 equally spaced pressure levels between 1000 and 100 mb, with the exception of RH, which is set to zero above 300 mb. The presence of topography is not considered; data are defined at all pressure levels in the domain. The horizontal domain extends from 20° to 55°N and from 110° to 60°W. We interpolate these analyses bilinearly in the horizontal to an unstaggered grid on a Lambert conformal projection centered at 37.5°N, 85.0°W and true at 30° and 60°N. The grid contains 34 × 36 points in the x and y directions; the horizontal spacing is 100 km.

The dataset for the M case is extracted from NMC global objective analyses on a 2.5° latitude–longitude grid archived at the National Center for Atmospheric Research. These analyses consist of h, T, and $\mathbf{V}$ on the 10 mandatory pressure levels between 1000 and 100 mb, and RH on the six mandatory pressure levels between 1000 and 300 mb. We extract data for the sector bounded between 20° and 55°N and between 110° and 60°W and linearly interpolate with respect to the logarithm of pressure to obtain analyses at 900, 800, and 600 mb, yielding a dataset at 10 equally spaced pressure levels between 1000 and 100 mb. We interpolate these analyses bilinearly in the horizontal to an unstaggered grid on a Lambert conformal projection centered at 37.5°N, 85.0°W and true at 30° and 60°N. The grid contains 17 × 17 points in the x and y directions; the horizontal spacing is 200 km. It is recognized that such a coarse-resolution analysis can be expected to resolve mesoscale structure only to a minimal extent. Although we view this limitation to be acceptable for the purpose of illustrating the psi-vector methodology, it precludes detailed analysis and interpretation of ageostrophic circulations in the vicinity of upper-level jet–front systems in the M case.

We proceed to review computational procedures applicable to both the PD and M cases, referring to the methodology presented in section 2. First, $\mathbf{V}_g$ is calculated from h at all points on the unstaggered grid, using centered finite differences in the interior and one-sided differences on the lateral boundaries. The Coriolis parameter f_0, determined from the latitude of the center of the domain (37.5°N), is 8.88×10^{-5} s^{-1} in both cases. The ageostrophic wind $\mathbf{V}_{ag}$ is then evaluated at all points on the unstaggered grid.

Next, $\mathbf{V}_{ag}$ is partitioned according to (2.5) using the version of the staggered grid described by Lynch (1989) applicable to the case where the tangential wind component is specified on the lateral boundaries.[3] The center points and dimensions of the staggered grids used in the PD and M cases coincide with those of the unstaggered grids adopted for these respective cases. Following bilinear interpolation of $\mathbf{V}_{ag}$ to the staggered grid, we calculate ζ_{ag} and δ_{ag} from $\mathbf{V}_{ag}$ on the staggered grid using (2.12) and the left-hand side of (2.2). We then invert (2.10) and (2.11) numerically[4] for Ψ_r and Φ_d, using homogeneous Dirichlet conditions on the lateral boundaries. Determination of Ψ_r and Φ_d yields $\mathbf{V}_{agr}$ and $\mathbf{V}_{agd}$ from (2.8) and (2.9). The following step of the procedure for partitioning $\mathbf{V}_{ag}$ is to solve for Φ_h from the first member of (2.7) with the lateral boundary conditions given by (2.15). This yields $\mathbf{V}_{agh}$ through the first member of (2.6), completing the partition in (2.5). Finally, the various parts of the ageostrophic wind are bilinearly interpolated to the unstaggered grid for display purposes; a step necessitated by the positioning of u_{ag} and v_{ag} at separate sets of points on the staggered grid.

The accuracy of the partition of $\mathbf{V}_{ag}$ is checked by comparing $\mathbf{V}_{ag}$ interpolated to the staggered grid with the sum of its harmonic, rotational, and divergent parts, as determined on the staggered grid; this sum is referred to as the "recovered" $\mathbf{V}_{ag}$. The rms vector differences in column A of Table 1 indicate that the recovery of $\mathbf{V}_{ag}$ at all levels in the PD and M cases is essentially within single-precision machine accuracy, as expected for the staggered grid described by Lynch (1989). Overall rms vector differences are slightly in excess of a factor of 6 greater for the PD case than for the M case, presumably because the ageostrophic winds are larger in magnitude in a domain-averaged sense in the former case. (The $\mathbf{V}_{ag}$ patterns for the PD and M cases may be compared at 300 mb by looking ahead to Figs. 5a and 12a.) This degree of accuracy is compromised, however, by interpolating $\mathbf{V}_{ag}$ back to the unstaggered grid for display purposes, which introduces a characteristic rms vector difference somewhat in excess of 0.5 m s^{-1} (Table 1, column B). This comparison is illustrated for the PD case in Fig. 1. The input $\mathbf{V}_{ag}$ on the unstaggered grid (referred to as "analyzed") is shown at 800 and 300 mb in Figs. 1a,c; the vector difference between the recovered $\mathbf{V}_{ag}$ interpolated back to the unstaggered grid and the analyzed $\mathbf{V}_{ag}$ is shown at the same levels in Figs. 1b,d. (For additional reference, the recovered $\mathbf{V}_{ag}$ fields for the PD case at 800 and 300 mb

[3] The use of the staggered grids described by Lynch (1989) allows the exact recovery (within roundoff error) of a two-dimensional vector field on a limited-area domain. This degree of accuracy is not possible with an unstaggered grid for reasons enumerated by Lynch (1988).

[4] Inversion of (2.10) and (2.11), as well as (2.7), (2.18), and (2.24), is accomplished using successive overrelaxation (e.g., Haltiner and Williams 1980, section 5.10.1) in single precision on a VAX 3500 class computer.

TABLE 1. Root-mean-square (rms) vector differences (m s^{-1}) for various ageostrophic wind components for the Presidents' Day (1200 UTC 19 February 1979) and the Megalopolitan (1200 UTC 11 February 1983) storms. The rms vector differences are listed for individual pressure levels [p (mb)] and for the entire domain (the latter denoted by "3D"). Column A: rms vector difference between analyzed $\mathbf{V}_{ag}$ interpolated to the staggered grid and $\mathbf{V}_{ag}$ recovered on the staggered grid using unadjusted horizontal divergence. Column B: rms vector difference between recovered $\mathbf{V}_{ag}$ interpolated to the unstaggered grid and analyzed $\mathbf{V}_{ag}$ on the unstaggered grid. Column C: rms vector difference between $\mathbf{V}_{agd}$ diagnosed from Φ_d on the staggered grid using unadjusted horizontal divergence and then interpolated to the unstaggered grid, and $\mathbf{V}_{agd}$ diagnosed from ψ on the unstaggered grid using adjusted horizontal divergence.

Date	p (mb)	A ($\times 10^{-4}$)	B ($\times 10^{0}$)	C ($\times 10^{0}$)
1200 UTC	1000	0.50395	1.11024	2.04999
19 Feb 1979	900	0.19286	0.55133	1.72660
	800	0.19574	0.47990	1.50933
	700	0.34699	0.33212	1.65463
	600	0.51723	0.46650	1.50224
	500	0.56921	0.49569	1.66306
	400	0.52056	0.45906	1.68561
	300	0.96754	0.59443	2.08133
	200	1.0827	0.73653	2.34479
	100	1.3036	0.88983	2.59985
	3D	0.71555	0.65107	1.91448
1200 UTC	1000	0.095227	0.52439	1.51081
11 Feb 1983	900	0.020570	0.32650	0.38448
	800	0.059075	0.29647	0.33956
	700	0.042761	0.26909	0.40178
	600	0.074263	0.28561	0.20972
	500	0.10410	0.38882	0.27938
	400	0.14735	0.56138	0.61537
	300	0.10587	0.75368	1.11939
	200	0.15047	0.85058	0.61348
	100	0.22332	0.60546	0.66448
	3D	0.11687	0.52420	0.72655

interpolated back to the unstaggered grid are shown later in Figs. 4a and 5a.) Consistent with the rms statistics, characteristic magnitudes of the vector differences in ageostrophic wind are less than about 1 m s^{-1} over most of the domain at both levels, with differences tending to be larger in regions where $\mathbf{V}_{ag}$ is strong and/or varies rapidly [e.g., in the vicinity of the closed low at 800 mb centered over southeastern Virginia (Figs. 1a,b)].

Following the partition of $\mathbf{V}_{ag}$, we determine the kinematic vertical motion ω on the unstaggered grid following the well-known approach of O'Brien (1970), given the constant-f ageostrophic wind. Neglecting the influence of terrain, we assume that ω vanishes at the lower boundary (p_b = 1000 mb) and integrate the continuity equation (2.2) upward, applying a linear correction to the horizontal divergence to ensure that ω vanishes at the upper boundary (p_t = 100 mb). Given the three-dimensional distribution of ω, (2.18) is inverted for χ subject to homogeneous Dirichlet conditions on the lateral boundaries, ψ is diagnosed from (2.19a), and $\mathbf{V}_{agd}$ is determined from the first member of (2.17). The kinematically derived ω field also is used to provide lateral boundary conditions when solving the QG omega equation (2.24), which is performed on the unstaggered grid in conjunction with Dirichlet conditions (homogeneous at 1000 and 100 mb and nonhomogeneous at the lateral boundaries).

As mentioned in section 2c, $\mathbf{V}_{agd}$ determined from (2.17) may be compared with $\mathbf{V}_{agd}$ determined from (2.9). It should be recognized that these two methods of calculating $\mathbf{V}_{agd}$ will not yield equivalent results. First, $\mathbf{V}_{agd}$ determined from (2.9) requires knowledge of δ_{ag}, which is derived from $\mathbf{V}_{ag}$ interpolated to the staggered grid from the unstaggered grid. The resulting $\mathbf{V}_{agd}$ field then must be interpolated back to the unstaggered grid for comparison with the $\mathbf{V}_{agd}$ field determined from (2.17). A second source of the discrepancy between the two $\mathbf{V}_{agd}$ fields is that the computation of vertical motion using the O'Brien (1970) procedure results in modification of the horizontal divergence on the unstaggered grid in order to meet the requirement of $\omega = 0$ at the upper boundary. Thus, the $\mathbf{V}_{agd}$ field derived from (2.17) is consistent with a different horizontal divergence field from that used in inverting (2.11). Examples of $\mathbf{V}_{agd}$ determined from (2.9), along with its vector difference with $\mathbf{V}_{agd}$ determined from (2.17), are shown for the PD case in Figs. 2a,b (800 mb) and Figs. 2c,d (300 mb). Magnitudes of vector differences are relatively large (in excess of 2 m s^{-1}) in the eastern portion of the domain at both levels, corresponding to the presence of a well-defined divergent ageostrophic circulation in this area.

Characteristic rms vector differences between the two $\mathbf{V}_{agd}$ fields for the PD and M cases are about 2 and 0.7 m s^{-1}, respectively (Table 1, column C). The rms vector differences for both cases exceed their respective counterparts associated with the interpolation procedure (Table 1, column B), with the relative increase significantly larger for the PD case than for the M case. The larger differences in the PD case reflect, in part, stronger divergent ageostrophic circulations relative to the M case [e.g., compare the 300-mb $\mathbf{V}_{agd}$ and Φ_d fields in Figs. 2c (PD case) and 12e (M case)]; stronger divergent ageostrophic circulations are consistent with the finer-resolution grid in the PD case (100 km compared with 200-km spacing) and the different analysis procedures utilized in the two cases. The larger rms vector difference between the $\mathbf{V}_{agd}$ fields in the PD case also is consistent with a larger correction to the horizontal divergence field, quite likely arising from the subjective nature of the analysis procedure in this case. [Note the monotonic increase with height of the rms vector differences above 600 mb in the PD case in column C of Table 1, and the larger magnitude of the vector difference along the eastern boundary of the domain between 30° and 40°N at 300 mb (Fig. 2d) compared with 800 mb (Fig. 2b).]

We conclude this section with a review of considerations arising in the construction of vertical cross sec-

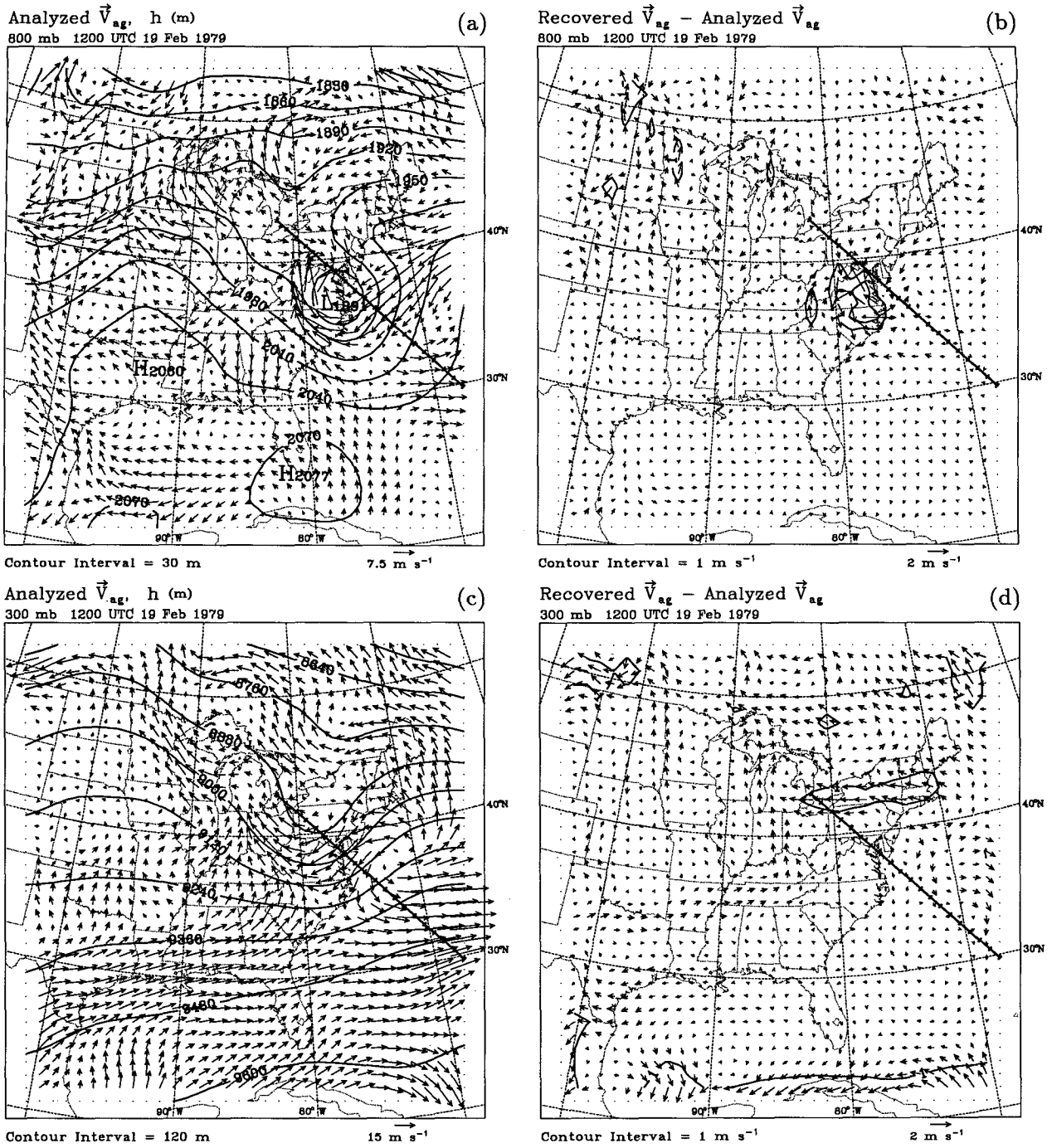

FIG. 1. Charts of analyzed $\mathbf{V}_{ag}$ and h and of the vector difference between recovered and analyzed $\mathbf{V}_{ag}$ at 1200 UTC 19 February 1979: (a) analyzed $\mathbf{V}_{ag}$ and h (contour interval 30 m) at 800 mb; (b) recovered minus analyzed $\mathbf{V}_{ag}$ and isotachs of vector difference (contour interval 1 m s^{-1}, zero contours suppressed) at 800 mb; (c) analyzed $\mathbf{V}_{ag}$ and h (contour interval 120 m) at 300 mb; (d) recovered minus analyzed $\mathbf{V}_{ag}$ and isotachs of vector difference (contour interval 1 m s^{-1}, zero contours suppressed) at 300 mb. The heavy, solid, straight lines on these and subsequent constant-pressure charts at 1200 UTC 19 February 1979 indicate orientation of cross sections to be shown for the Presidents' Day storm (Figs. 8–10). The grid distance between adjacent tick marks is 100 km.

tions. When ω_s and ω_n (2.23a,b) are displayed in cross section format, partial derivatives with respect to x and y are calculated on the unstaggered grid and then bilinearly interpolated to the coordinates of the cross section, which are equally spaced along a straight line on the conformal map projection. The expressions in

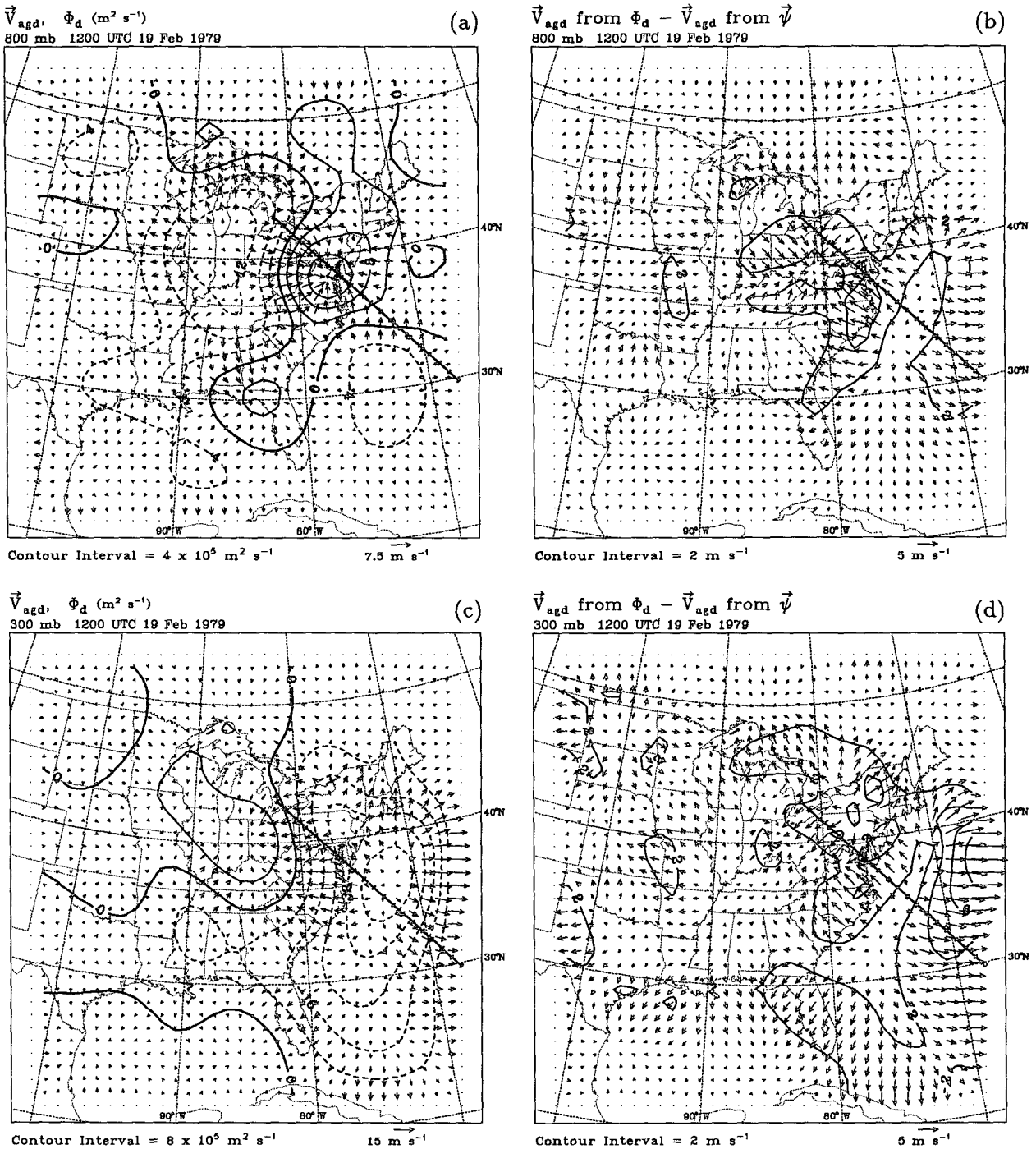

FIG. 2. Charts of $\mathbf{V}_{agd}$ diagnosed from Φ_d and of the vector difference between $\mathbf{V}_{agd}$ diagnosed from Φ_d and from ψ at 1200 UTC 19 February 1979: (a) $\mathbf{V}_{agd}$ diagnosed from Φ_d, and Φ_d (contour interval 4 × 10^5 m^2 s^{-1}) at 800 mb; (b) $\mathbf{V}_{agd}$ diagnosed from Φ_d minus $\mathbf{V}_{agd}$ diagnosed from ψ, and isotachs of vector difference (contour interval 2 m s^{-1}, zero contours suppressed) at 800 mb; (c) $\mathbf{V}_{agd}$ diagnosed from Φ_d, and Φ_d (contour interval 8 × 10^5 m^2 s^{-1}) at 300 mb; (d) $\mathbf{V}_{agd}$ diagnosed from Φ_d minus $\mathbf{V}_{agd}$ diagnosed from ψ, and isotachs of vector difference (contour interval 2 m s^{-1}, zero contours suppressed) at 300 mb.

(2.23a) and (2.23b) are then evaluated at each of the cross section coordinates. The same procedure of interpolating the x and y components to the cross section line and then applying the rotation formula (2.21a) is invoked when projecting the following vector quantities onto the cross section (s, p) plane: ψ, $\mathbf{V}_{agd}$ [deter-

mined from (2.17)], $\mathbf{V}_{ag}$, $\mathbf{V}$, and the horizontal components of ζ_a (2.27).

When displaying velocity vectors in cross section format, it is necessary for the vertical component ω to be scaled relative to the horizontal component v_s in order to maintain tangency of a streamline or trajectory at the location of the vector. The scale factor for a cross section in which the ordinate is linear in pressure, derived from considering the continuity equation in the (s, p) plane, is given by $-\gamma S(p_b - p_t)^{-1}$, where γ is the aspect ratio (height divided by width) of the cross section plot, S is the distance on the grid corresponding to the cross section width, and p_b (1000 mb) and p_t (100 mb) are the pressures at the bottom and top of the cross section, respectively.[5] For all cross sections of velocity to be presented, the scale factor is -2.444 m μb^{-1}. For displays of the projection of absolute vector vorticity (2.27) onto the (s, p) plane, the same scale factor applies without the minus sign.

4. Diagnosis of ageostrophic circulations for the Presidents' Day and Megalopolitan storms

Consistent with the objective of modifying the diagnostic methodology of KSD into a form suitable for real-data applications, we do not attempt extensive case studies of the Presidents' Day (PD) and Megalopolitan (M) storms from an ageostrophic-circulation perspective. The reader is referred to Bosart (1981), Uccellini et al. (1984, 1985), and Kocin and Uccellini (1990, section 7.18) for comprehensive synoptic overviews of the PD case and to Sanders and Bosart (1985), Uccellini and Kocin (1987, hereafter referred to as UK), and Kocin and Uccellini (1990, section 7.20) for the M case. In the PD case, we focus on the ageostrophic circulations in the vicinity of an upper-level jet streak located near the base of a short-wave trough at 1200 UTC 19 February 1979. In the M case, we perform a similar diagnosis for the area between jet maxima located, respectively, within the base of a trough southwest of a surface cyclone and within a confluence zone northeast of this cyclone at 1200 UTC 11 February 1983. The reader is referred to Figs. 1 and 16 of UK, Fig. 21 of Kocin and Uccellini (1990), and to Fig. 1 of Hakim and Uccellini (1992) for schematic illustrations of this configuration of "laterally coupled" jets.

a. Presidents' Day storm: 1200 UTC 19 February 1979

Figures 3a–c present a bottom-up illustration of the main flow features of the PD case at 1200 UTC 19 February 1979 (12/19). A well-defined cyclonic vortex at 1000 mb, embedded within a strip of enhanced coastal baroclinicity, is centered just off southeastern Virginia. This cyclone is intensifying rapidly beneath the inflection of a negatively tilted diffluent short-wave trough at 500 mb and the left exit of a strong ($\sim$75 m s^{-1}) cyclonically curved jet streak at 300 mb. Lower- and upper-level depictions of the partitioned ageostrophic winds at 12/19 are presented in Figs. 4 (800 mb) and 5 (300 mb), respectively; the divergent ageostrophic parts are not included since they already have been presented in Figs. 2a (800 mb) and 2c (300 mb). In the following discussion, we will focus primarily on the ageostrophic wind patterns in the vicinity of the low-level cyclone and upper-level jet streak.

The total $\mathbf{V}_{ag}$ field[6] at 800 mb is shown in Fig. 4a. Anticyclonic ageostrophic flow is evident around the cyclone center and in the neighborhood of the low-amplitude trough along 80°W north of Lake Huron. The anticyclonic character of $\mathbf{V}_{ag}$ in these regions is consistent with gradient wind balance in cylonically curved flow, which requires the total wind to be subgeostrophic (e.g., Holton 1992, section 3.2.5).[7] The total $\mathbf{V}_{ag}$ field in the vicinity of the cyclone and northern trough, as well as elsewhere in the diagnostic domain, is reproduced qualitatively by its nondivergent part $\mathbf{V}_{agnd}$ (Fig. 4b). Further separation of $\mathbf{V}_{agnd}$ into its harmonic (Fig. 4c) and rotational (Fig. 4d) parts reveals the dominance of the latter in explaining the anticyclonic ageostrophic flow around the cyclone center and northern trough; both of these features correspond to maxima of streamfunction Ψ_r in Fig. 4d. The contribution of the harmonic part is significant only near the boundaries; its influence in the vicinity of the cyclone, as well as along the cross section to be discussed later in this subsection, is relatively minor. The divergent part of $\mathbf{V}_{ag}$ and the corresponding velocity potential field Φ_d (Fig. 2a) indicate regions of well-defined outflow corresponding approximately to the center of the anticyclone at 1000 mb (Fig. 3a) and inflow centered just to the northwest of the center of the cyclone at 1000 and at 800 mb (Fig. 4a). The location of the center of inflow at 800 mb (Fig. 2a), coinciding with the maximum of Φ_d, matches closely with the area of heavy snow evident in Fig. 4 of Bosart (1981) and of mod-

[5] The scale factor considered here does not account for map scale factors; were this level of elaboration to be adopted, it would be necessary to display $(v_s/m, \omega/m)$ and to reinterpret S as earth-relative distance.

[6] The recovered $\mathbf{V}_{ag}$ field is shown in Figs. 4a and 5a rather than its analyzed counterpart, since the former technically corresponds to the sum of the partitioned components on the staggered grid, all of which are interpolated to the unstaggered grid for display in Figs. 4 and 5.

[7] Qualitative arguments presented in this paper relating the along-stream ageostrophic wind to flow curvature assume that the contribution of the second term on the right-hand side of (2.3) to momentum balance in the cross-stream direction can be neglected. This approximation should be well satisfied for features located close to the latitude of the center point of both domains (37.5°N).

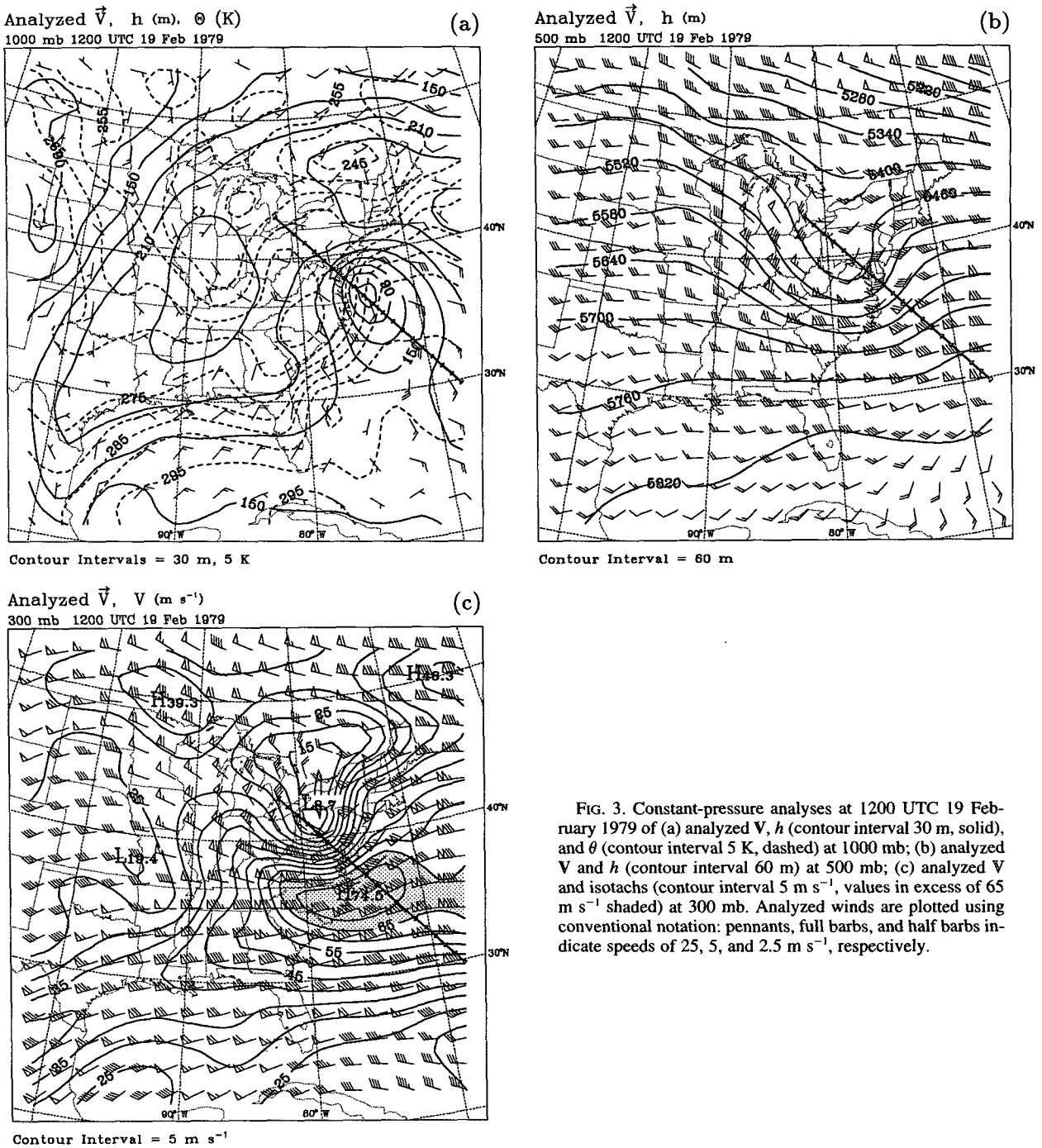

FIG. 3. Constant-pressure analyses at 1200 UTC 19 February 1979 of (a) analyzed **V**, h (contour interval 30 m, solid), and θ (contour interval 5 K, dashed) at 1000 mb; (b) analyzed **V** and h (contour interval 60 m) at 500 mb; (c) analyzed **V** and isotachs (contour interval 5 m s^{-1}, values in excess of 65 m s^{-1} shaded) at 300 mb. Analyzed winds are plotted using conventional notation: pennants, full barbs, and half barbs indicate speeds of 25, 5, and 2.5 m s^{-1}, respectively.

erate to heavy precipitation shown in Fig. 1 of Uccellini et al. (1984).

At 300 mb, the total $\mathbf{V}_{ag}$ field (Fig. 5a) exhibits upstream-directed ageostrophic flow in the short-wave trough, indicative of subgeostrophic flow. The upstream component of $\mathbf{V}_{ag}$ is best defined in the channel bounded by the 8880- and 9000-m geopotential height contours, coinciding with the strongest cyclonic curvature of the short-wave trough. This channel is situated just north of the jet streak, the core of which is located over eastern North Carolina (Fig. 3c). Cross-contour ageostrophic flow toward lower geopotential height is evident over the Carolinas west of 80°W, coinciding with the jet entrance region, and toward higher geopotential height off the North Carolina coast, coinciding with the jet exit region (Fig. 5a). As at 800

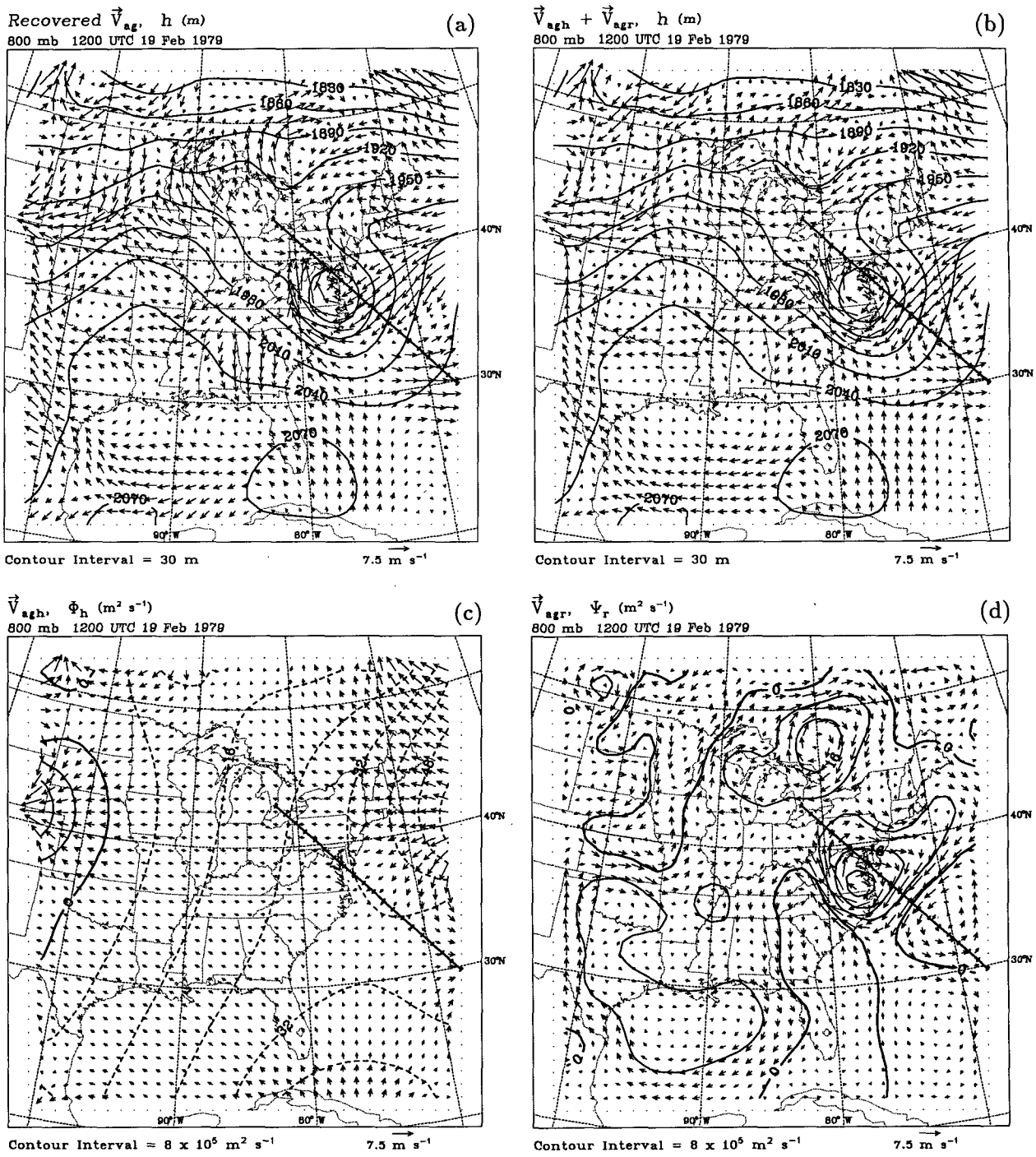

FIG. 4. Charts of recovered $\mathbf{V}_{ag}$ at 800 mb and its nondivergent ($\mathbf{V}_{agh}$ + $\mathbf{V}_{agr}$), harmonic ($\mathbf{V}_{agh}$), and rotational ($\mathbf{V}_{agr}$) components at 1200 UTC 19 February 1979: (a) recovered $\mathbf{V}_{ag}$ and h (contour interval 30 m); (b) $\mathbf{V}_{agh}$ + $\mathbf{V}_{agr}$ and h (contour interval 30 m); (c) $\mathbf{V}_{agh}$ and Φ_h (contour interval 8 × 10^5 m^2 s^{-1}); (d) $\mathbf{V}_{agr}$ and Ψ_r (contour interval 8 × 10^5 m^2 s^{-1}).

mb, the total $\mathbf{V}_{ag}$ pattern is reproduced qualitatively by its nondivergent part over the entire domain at 300 mb (Fig. 5b). The influence of the harmonic part (Fig. 5c) is more extensive than at 800 mb (Fig. 4c), although its contribution to the total $\mathbf{V}_{ag}$ pattern in the immediate vicinity of the short wave and jet streak is relatively minor. The major features of the $\mathbf{V}_{agr}$ and Ψ_r patterns in this region (Fig. 5d) are an anticyclonic gyre cen-

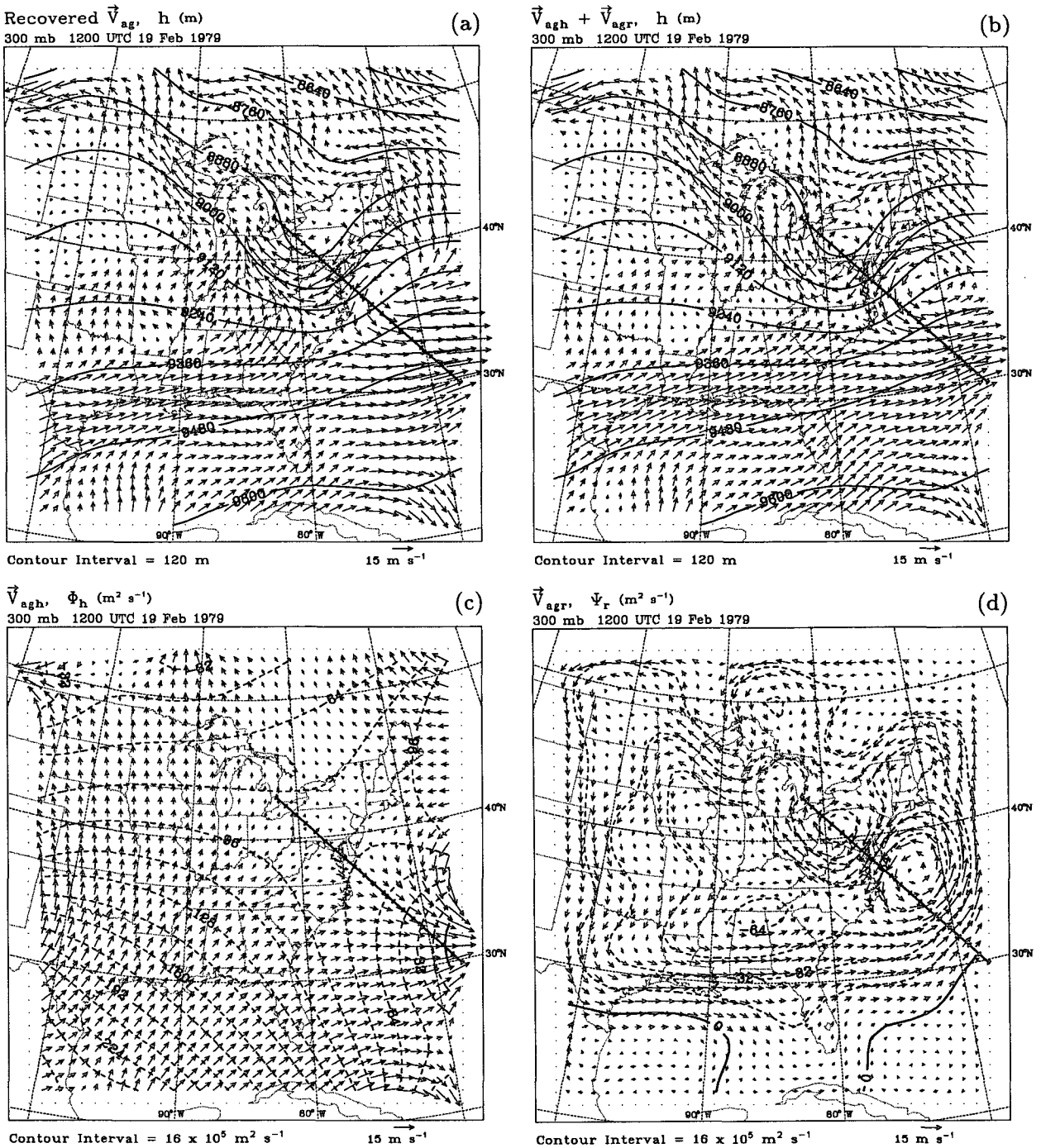

FIG. 5. Charts of recovered $\mathbf{V}_{ag}$ at 300 mb and its nondivergent ($\mathbf{V}_{agh} + \mathbf{V}_{agr}$), harmonic ($\mathbf{V}_{agh}$), and rotational ($\mathbf{V}_{agr}$) components at 1200 UTC 19 February 1979: (a) recovered $\mathbf{V}_{ag}$ and h (contour interval 120 m); (b) $\mathbf{V}_{agh} + \mathbf{V}_{agr}$ and h (contour interval 120 m); (c) $\mathbf{V}_{agh}$ and Φ_h (contour interval 16×10^5 m^2 s^{-1}); (d) $\mathbf{V}_{agr}$ and Ψ_r (contour interval 16×10^5 m^2 s^{-1}).

tered over western Pennsylvania and cyclonic gyres centered over northern Alabama and off the Virginia coast. These three features combine to yield the upstream-directed ageostrophic flow in the base of the short-wave trough and the cross-contour ageostrophic flow in the jet entrance and exit regions. Nevertheless, despite the qualitative recovery of the total $\mathbf{V}_{ag}$ pattern by $\mathbf{V}_{agnd}$ at 300 mb, comparison of Figs. 5a, 5b, and 5d indicates that the upstream-directed component of $\mathbf{V}_{ag}$ in the trough base and the cross-contour component of

$\mathbf{V}_{ag}$ in the jet entrance region are underestimated by $\mathbf{V}_{agnd}$ and $\mathbf{V}_{agr}$; the deficit in both of these areas is made up by $\mathbf{V}_{agd}$ (Fig. 2c).

The patterns of $\mathbf{V}_{agd}$ and Φ_d at 300 mb (Fig. 2c) feature well-defined centers of divergent inflow and outflow; these respective centers are located above the regions of outflow and inflow at 800 mb (Fig. 2a) and correspond approximately to the centers of the anticyclone and cyclone at 1000 mb (Fig. 3a). The centers of divergent inflow and outflow at 300 mb also are closely coincident with the northwesterly and southwesterly flow infections in the 300-mb geopotential height field (Fig. 5a). The vertical configuration of the $\mathbf{V}_{agd}$ and Φ_d patterns is indicative of two-layer divergent circulation patterns associated with the short-wave trough, consistent with kinematic descriptions of the vertical circulation patterns accompanying idealized baroclinic wave disturbances (e.g., compare the $\mathbf{V}_{agd}$ patterns in Figs. 2a,c with their counterparts in Figs. 7b,d of KSD).

The kinematically derived ω and ψ patterns at 800 (Fig. 6a) and 500 mb (Fig. 6b) show that the vertical branches of the above-described circulation patterns consist of descent centered over Kentucky and ascent centered over the Delmarva Peninsula. [For interpretation of the relationship between ψ, $\mathbf{V}_{agd}$, and ω in a two-layer vertical circulation, refer to (2.17) and Fig. 1 of KSD.] The centers of descent and ascent overlap closely with the locations of the northwesterly and southwesterly flow inflections of the short-wave trough at 500 (Fig. 3b) and at 300 mb (Fig. 5a). These centers also are situated on the cyclonic-shear side of the jet streak at 300 mb (Fig. 3c), consistent with kinematically based descriptions of distributions of upper-tropospheric divergence and midtropospheric vertical motion in cyclonically curved jet streaks (e.g., Beebe and Bates 1955; Shapiro and Kennedy 1981; Keyser and Shapiro 1986, section 4b; Uccellini 1990, section 6.3.1; Moore and VanKnowe 1992).

A second prominent region of ascent is evident off the North Carolina coast at 800 mb (Fig. 6a); comparison with the 500-mb ω field (Fig. 6b) indicates this feature to be confined to the lower troposphere. This region of ascent coincides approximately to the position of a convective line, extending approximately along 74°W between 35° and 37°N according to the operational radar summary valid at 1235 UTC 19 February 1979 [refer to the discussion in section 7 of Bosart (1981) and to Fig. 3.12b of Loughe (1992)]. Evidence for a convective feature in this region is also found in infrared satellite imagery at 1200 UTC 19 February [see Fig. 2c of Uccellini et al. (1985)]. The absence of this ascent maximum in the adiabatic QG ω field at 800 mb (Fig. 7a) suggests the possible presence of a latent-heat-driven divergent circulation in this region. It is possible that the influence of this divergent circulation may be accounted for in the subjectively analyzed wind field, from which the kinematic ω field is derived, but not in the mass field, from which the QG ω field is derived. On the basis of these consider-

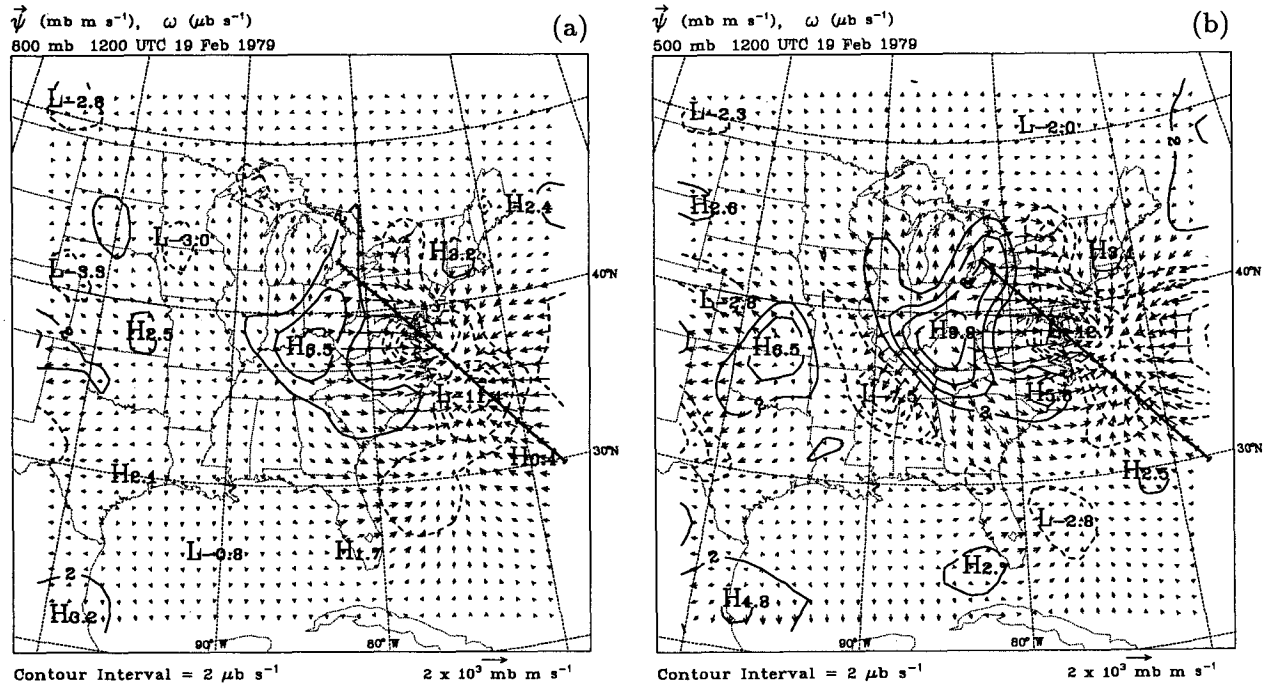

FIG. 6. Charts of ψ and kinematic ω (contour interval 2 μb s^{-1}, zero contours suppressed) at 1200 UTC 19 February 1979: (a) 800 mb; (b) 500 mb.

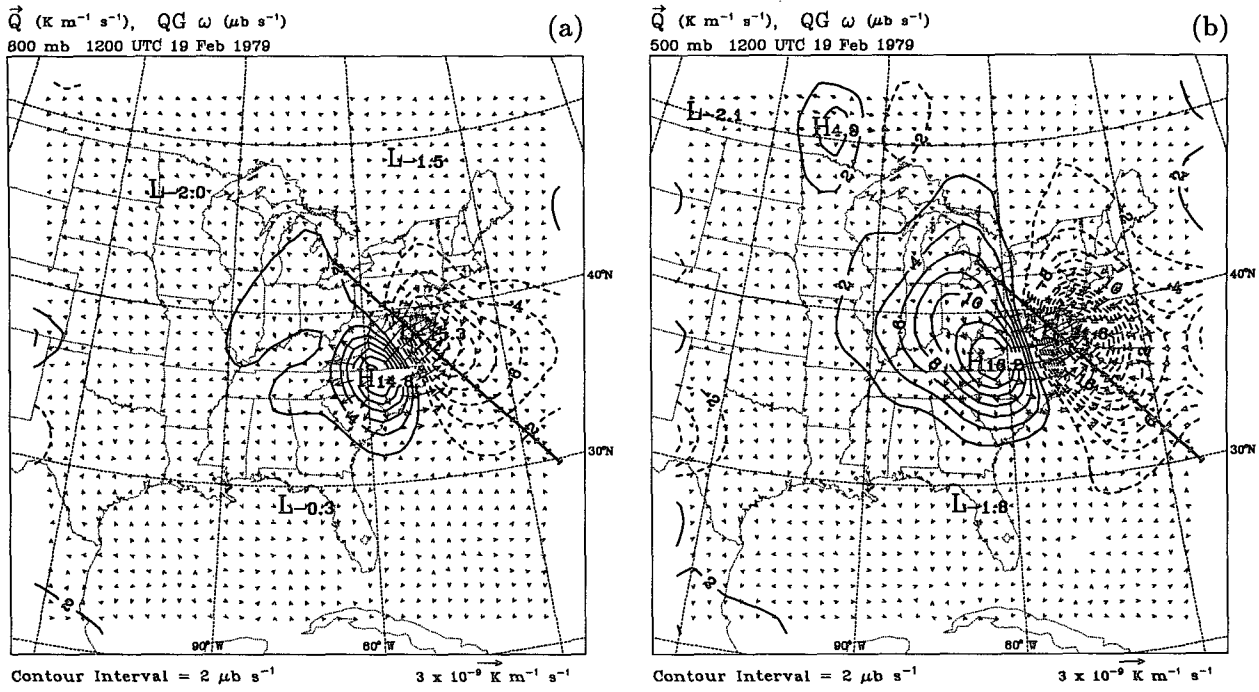

FIG. 7. Charts of Q and quasigeostrophic ω (contour interval 2 μb s^{-1}, zero contours suppressed) at 1200 UTC 19 February 1979: (a) 800 mb; (b) 500 mb.

ations, we hypothesize that the kinematic ascent maximum at 800 mb may be a manifestation of the convective line on the scale of the analysis, but further investigation of a dynamical relationship between these two features is beyond the scope of the present paper.

The distributions of kinematically derived ω and ψ are qualitatively consistent with the QG-derived distributions of ω and Q at 800 and 500 mb (Figs. 7a,b), although the mesoscale detail evident in the kinematic ω patterns is conspicuously absent from their QG counterparts. Also, the magnitudes of maximum descent and ascent in the kinematic ω patterns are less than those of their QG counterparts at both levels, consistent with expectations in regions of cyclonically curved flow [refer to section 3 of Keyser et al. (1992a)]. Finally, the spatial separation between the descent and ascent maxima in the kinematically derived ω fields is greater than that of their QG counterparts. The separation is smaller in the QG ω fields because the descent maxima are located closer to the vortex center at 800 mb and the short-wave trough axis at 500 mb. Consistent with this observation, the Q patterns at 800 and 500 mb appear to be closely tied to the vortex and short-wave trough at these respective levels (compare Figs. 7a,b with Figs. 4a and 3b). This discrepancy in location between the kinematic and QG descent maxima may be a reflection of the inability of the QG ω equation to expand and contract the spatial scales of regions of descent and ascent, assuming that the former and latter correspond to regions of small and large absolute vorticity, respectively (Hoskins 1975; Eliassen 1984). This limitation is a consequence of the horizontal invariance of the coefficients of the elliptic operator on the left-hand side of (2.24), which implies a symmetric response to idealized forcing consisting of a dipole composed of oppositely signed point sources.

Further discussion of this case is now presented for a cross section that intersects the kinematic ascent maxima at 800 and 500 mb (Figs. 6a,b) and the southwesterly flow inflection at 500 mb (Fig. 3b). For later reference, the cross section is located in the exit region of the 300-mb jet, just downstream of the jet core (Fig. 3c). A question to be pursued concerns the relative contributions of the divergent ageostrophic circulations in the cross- and alongstream directions [corresponding to tangential (s) and normal (n) to the cross section] to the ascent maxima located within the southwesterly flow inflection. The wind component normal to the cross section v_n (Fig. 8a) reveals the presence of the 300-mb jet directly above the convective line discussed earlier. There is strong cyclonic shear associated with the coastal cyclone and with the upper-level jet.

The distribution of PV_e (Fig. 8b) and the projection of ζ_a onto the cross-sectional plane superimposed on θ_e (Fig. 8c) show that PV_e is small and near zero between 800 and 400 mb above the area of moderate to heavy snow. (Note the approximate coincidence of the projected absolute vorticity vectors and θ_e in this region.) The overlap of the region of small PV_e with high relative humidity [here, RH > 70% (denoted by shading

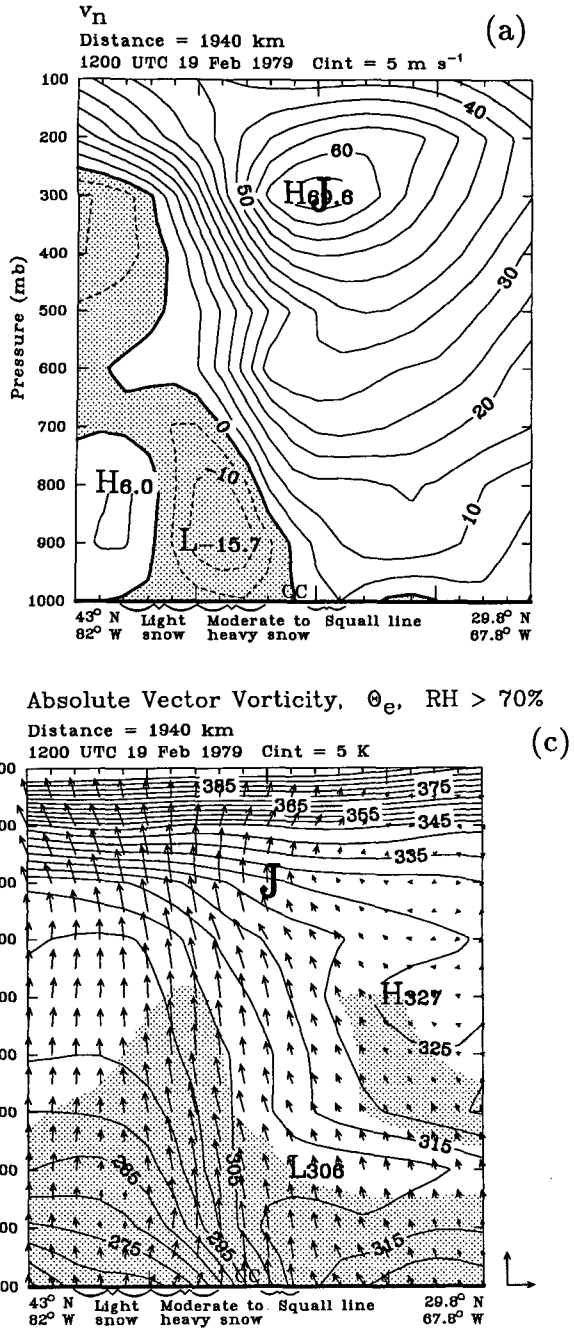

FIG. 8. Cross sections at 1200 UTC 19 February 1979 of (a) v_n (contour interval 5 m s^{-1}, negative values shaded); (b) PV_e [contour interval 0.5 PVU (1 PVU = 1×10^{-6} m^2 K kg^{-1} s^{-1})] and RH (values in excess of 70% shaded); (c) projection of ζ_a onto the cross-sectional plane, θ_e (contour interval 5 K), and RH (values in excess of 70% shaded). In these and subsequent cross sections shown at 1200 UTC 19 February 1979 (Figs. 9 and 10), latitude–longitude endpoints of the cross section, upper-level jet (J), regions of precipitation, and surface cyclone center (CC) are indicated. The distance between tick marks on the cross section abscissa is 100 km measured with respect to the grid; the total distance of 1940 km, indicated in the title block, is measured with respect to the earth. In (a), negative (positive) values denote flow out of (into) the page. In (c), the magnitudes of the vertical and horizontal scales of the reference vector are 27.16×10^{-5} s^{-1} and 54.31×10^{-5} m s^{-1} μb^{-1}, respectively.

in Figs. 8b,c) is taken to be a crude indicator of possible saturation] is suggestive of slantwise neutrality, consistent with considerations expressed previously in section 2d. Relatively high values of PV_e are found below 800 mb in association with cyclonic shear and convective stability ($-\partial\theta_e/\partial p > 0$) above and northwestward of the cyclone center, and negative values of PV_e exist below 800 mb southeastward of the convective line in a region of convective instability ($-\partial\theta_e/\partial p < 0$).

Three representations of transverse vertical circulations are presented in Fig. 9. (These correspond to entries 1, 2, and 5 in Table 1 of KSD.) Both the (v_s, ω) (Fig. 9a) and the (v_{ags}, ω) (Fig. 9b) representations reveal strong ascent above the region of moderate to heavy snowfall and southeastward of the convective line. In the former representation (Fig. 9a), there is the suggestion of branching of the ascent plume, with slantwise ascent over the region of moderate to heavy snow and upright ascent to the southeast of the convective line. This description is compatible with expectations regarding airflow patterns associated with stratiform precipitation in baroclinic systems and with convective precip-

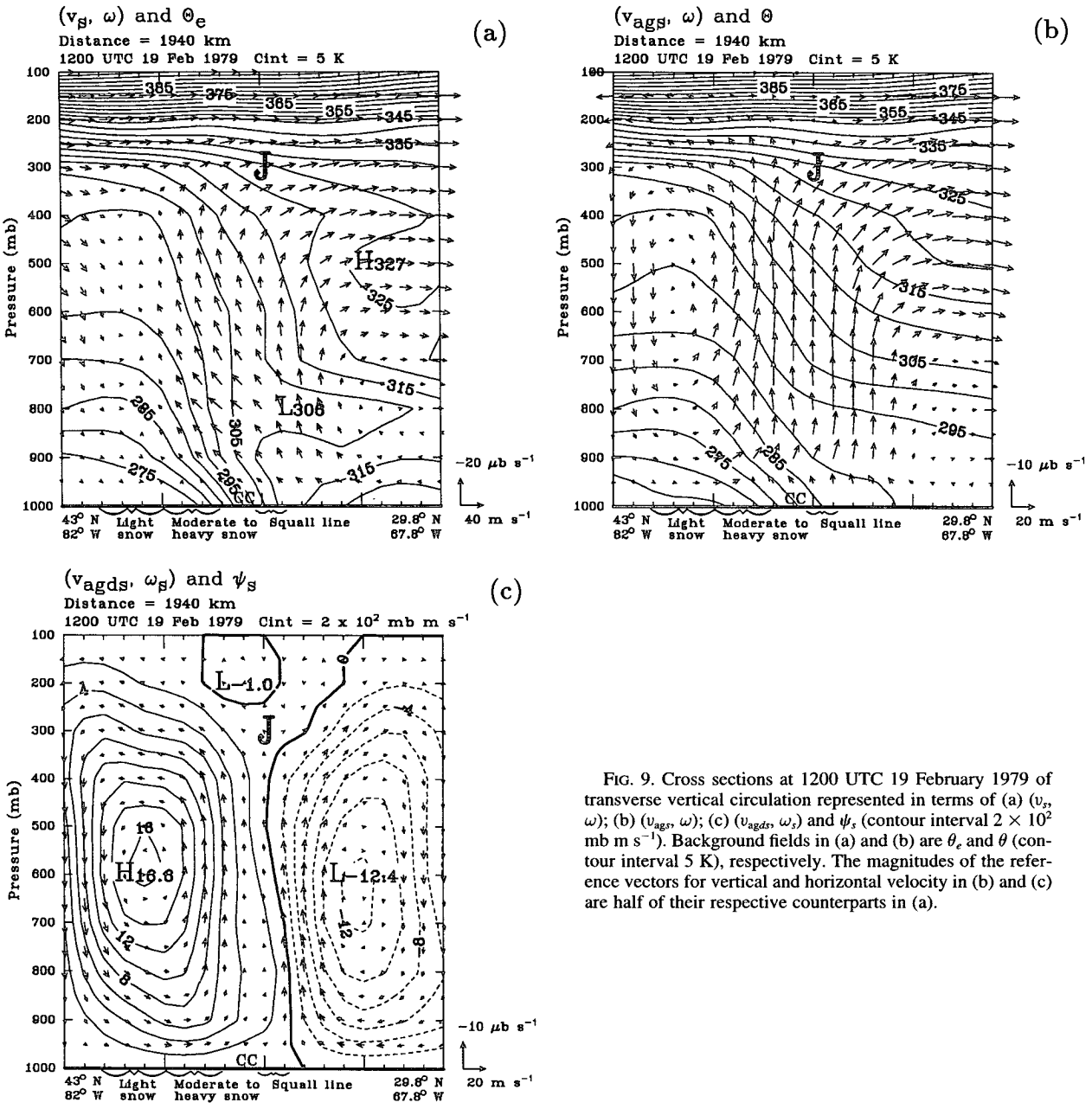

FIG. 9. Cross sections at 1200 UTC 19 February 1979 of transverse vertical circulation represented in terms of (a) (v_s, ω); (b) (v_{ags}, ω); (c) (v_{agds}, ω_s) and ψ_s (contour interval 2×10^2 mb m s^{-1}). Background fields in (a) and (b) are θ_e and θ (contour interval 5 K), respectively. The magnitudes of the reference vectors for vertical and horizontal velocity in (b) and (c) are half of their respective counterparts in (a).

itation, where it is understood that the (v_s, ω) representation corresponds to the projection of parcel trajectories onto the cross-sectional plane for steady, two-dimensional flow. In the latter representation (Fig. 9b), the circulation pattern hints at the presence of adjacent direct and indirect circulation cells on the cyclonic- and anticyclonic-shear sides of the 300-mb jet. At the jet core, v_{ags} is directed toward the anticyclonic-shear side, consistent with the intersection of the cross section with the jet exit region. Close examination of this figure reveals the presence of the split updraft cited above in connection with the (v_s, ω) representation (Fig. 9a).

The existence of adjacent circulation cells and of a split updraft is much more apparent in the ψ-derived representation (v_{agds}, ω_s) (Fig. 9c). This comparison is pursued further in Fig. 10, which displays the total kinematic ω and its components associated with divergent ageostrophic flow tangential (ω_s) and normal (ω_n) to the plane of the cross section. The descent maximum adjacent to the northwestern boundary of the cross section and the split updraft (Fig. 10a) are associated with the divergent circulation tangential to the cross-sectional plane (Fig. 10b). Although the magnitude of maximum ascent in the ω_n component (Fig. 10c) some-

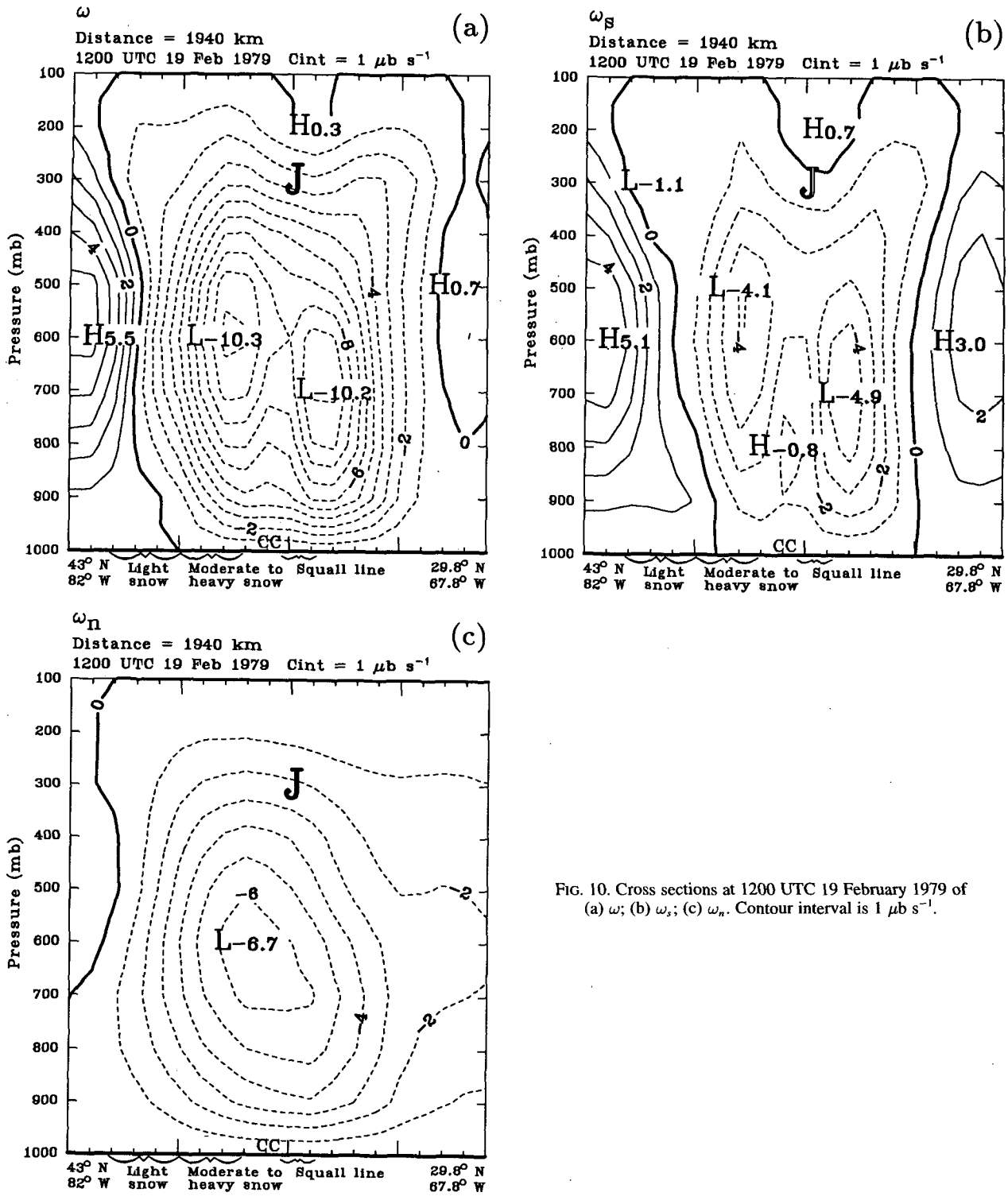

FIG. 10. Cross sections at 1200 UTC 19 February 1979 of (a) ω; (b) ω_s; (c) ω_n. Contour interval is 1 μb s^{-1}.

what exceeds that found in the ω_s component, the former is devoid of detailed (i.e., mesoscale) structure, possessing instead a synoptic-scale signature representative of the baroclinic wave. Thus, although the vertical circulation pattern sampled by the cross section is three-dimensional (as indicated by the comparable magnitudes of ω_s and ω_n), the divergent circulation tangential to the cross-sectional plane, represented by ω_s,

reveals localized maxima of ascent correlating with the regions of moderate to heavy snow and a convective line.

Finally, it is of interest that the ascent maximum in the ω_s pattern above the region of moderate to heavy snow is located to the northwest of the jet core (corresponding to the left exit region of the jet streak), whereas its counterpart in the ω_n pattern is located closer to the jet. These relative locations are consistent with the interpretation cited in the discussion of Fig. 6 in regard to the ascent maximum located over the Delmarva Peninsula. In this interpretation, ascent in the southwesterly flow inflection downstream of a cyclonically curved jet streak situated in the base of a shortwave trough may be viewed as a superposition of contributions from cross-stream divergent ageostrophic flow attributed to the jet streak, quantified by ω_s, and from alongstream divergent ageostrophic flow attributed to the baroclinic wave, quantified by ω_n [see Fig. 1 of Shapiro and Kennedy (1981) for a schematic of these component circulations]. This interpretation will be explored further in the summary section.

b. *Megalopolitan storm: 1200 UTC 11 February 1983*

The M case is of interest because of the hypothesized contributions to ascent from distinct vertical circulations associated with two laterally displaced jet streaks. The conceptual model of UK portrays adjacent direct and indirect ageostrophic circulations, based on the (v_{ags}, ω) definition, with the direct cell linked to confluence in the entrance region of the downstream jet and the indirect cell to diffluence in the exit region of the upstream jet. The question arises of the extent to which one may attribute the total vertical motion constituting the vertical branches of these circulation cells to divergent circulations in the cross-jet plane. The directional partition of the three-dimensional vertical circulation offered by the psi-vector formulation now will be applied to the M case to investigate this question.

At 1200 UTC 11 February 1983 (12/11), the 1000-mb analysis shows an anticyclone–cyclone pair oriented meridionally from Quebec to the Carolina coast, with a zonally oriented region of baroclinicity embedded within the confluence zone between the anticyclone and cyclone (Fig. 11a). At this time, the cyclone is intensifying below the left exit region of a jet maximum (Fig. 11b) and downstream of a trough axis (Fig. 12a) at 300 mb, both of which are located over the southeastern United States. The southern jet streak and exit region are better defined at 200 mb (Fig. 11c), suggesting a subtropical classification for this feature. Further inspection of Fig. 11b reveals a well-defined jet entrance region at 300 mb overlying the 1000-mb anticyclone, providing the second of the two jet features required by the UK conceptual model. At 12/11, precipitation is observed over the mid-Atlantic states, with the locus of heaviest activity over Virginia and West Virginia [refer to Fig. 6 of UK and to the radar summary for 1135 UTC 11 February 1983 reproduced in Fig. 4.1c of Loughe (1992)].

In the subsequent discussion of the horizontal distribution of $\mathbf{V}_{ag}$, we restrict attention to 300 mb, since the ageostrophic wind signatures in the conceptual model should be best defined at upper levels. There is cross-contour ageostrophic flow toward lower geopotential heights in the jet entrance region over New York and New England and toward higher geopotential heights in the jet exit region off the coast of Georgia and Florida (Fig. 12a). Upstream-directed ageostrophic flow is also apparent near the base of the trough over Kentucky and Tennessee. The pattern of total $\mathbf{V}_{ag}$ is replicated qualitatively by its nondivergent part (Fig. 12b), although the cross-contour ageostrophic flow is diminished in the jet entrance and exit regions, and the upstream-directed ageostrophic flow in the trough base is weaker as well. The distribution of $\mathbf{V}_{agnd}$ may be related to its constituent harmonic (Fig. 12c) and rotational (Fig. 12d) parts; comparison of these figures shows that the $\mathbf{V}_{agnd}$ field is composed of a prominent cyclonic gyre in $\mathbf{V}_{agr}$ centered over southeastern North Carolina, the influence of which extends over the entire diagnostic domain. The ageostrophic wind associated with this gyre contributes significantly to the cross-contour ageostrophic wind in the jet entrance and exit regions; note that the harmonic part is of minor consequence in these areas. Comparison of Figs. 12b and 12d shows that the main contribution of $\mathbf{V}_{agh}$ to $\mathbf{V}_{agnd}$ occurs in the vicinity of the lateral boundaries, especially the western and southern ones. The influence of $\mathbf{V}_{agh}$ is negligible along the cross section to be considered subsequently.

The above-cited discrepancies between the $\mathbf{V}_{ag}$ (Fig. 12a) and $\mathbf{V}_{agnd}$ (Fig. 12b) distributions in the jet entrance and exit regions, as well as in the trough base, are explained by $\mathbf{V}_{agd}$ (Fig. 12e), which features a widespread region of well-organized outflow centered over eastern Virginia and a corresponding region of diffuse inflow centered over northwestern Mississippi. In particular, the $\mathbf{V}_{agd}$ field associated with the outflow reinforces the cross-contour ageostrophic flow in the jet entrance and exit regions and the along-contour ageostrophic flow in the trough base. Consistent with the distribution of Φ_d (Fig. 12e), the kinematic ω and ψ patterns at 800 (Fig. 13a) and 500 mb (Fig. 13b) show a dipole of descent and ascent, the former centered over the southeastern United States and the latter along the mid-Atlantic coast in the inflection between the upstream trough and downstream confluence zone at 300 mb (Fig. 12a). Comparison of Figs. 13a and 13b suggests that the ascent maximum slopes upward toward colder air; the location and northwest–southeast alignment of the ascent maximum at 500 mb matches very well with the analyzed precipitation distribution shown in UK. The overall correspondence between the kinematic (Fig. 13) and the QG-diagnosed

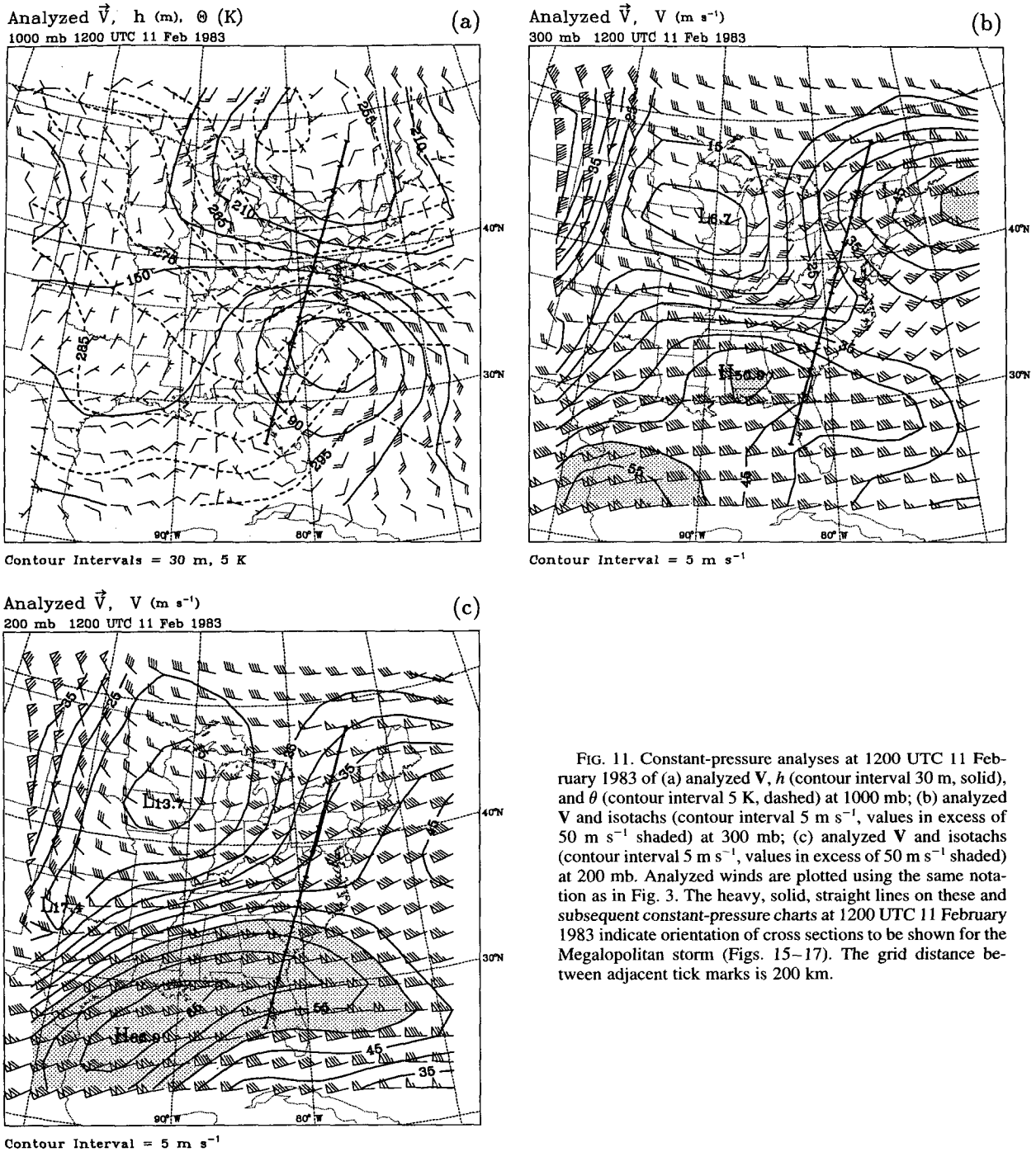

FIG. 11. Constant-pressure analyses at 1200 UTC 11 February 1983 of (a) analyzed **V**, h (contour interval 30 m, solid), and θ (contour interval 5 K, dashed) at 1000 mb; (b) analyzed **V** and isotachs (contour interval 5 m s^{-1}, values in excess of 50 m s^{-1} shaded) at 300 mb; (c) analyzed **V** and isotachs (contour interval 5 m s^{-1}, values in excess of 50 m s^{-1} shaded) at 200 mb. Analyzed winds are plotted using the same notation as in Fig. 3. The heavy, solid, straight lines on these and subsequent constant-pressure charts at 1200 UTC 11 February 1983 indicate orientation of cross sections to be shown for the Megalopolitan storm (Figs. 15–17). The grid distance between adjacent tick marks is 200 km.

ω fields (Fig. 14) is close; nevertheless, the QG-ascent maximum at 500 mb (Fig. 14b) appears more localized along the direction of the major axis of the ascent ellipse relative to its kinematic counterpart (Fig. 13b), more in agreement with the locus of heaviest precipitation over Virginia and West Virginia. The closer correspondence between the kinematic and QG ω fields in the present case compared with the PD case may be a consequence of smaller curvature in the present case (compare the 300-mb geopotential height patterns in Figs. 12a and 5a).

The cross section presented for the M case is oriented so as to intersect the entrance region of the northern jet and the exit region of the southern jet (Figs. 11b,c). This orientation is approximately normal to the major axis of the kinematic ascent region at 500 mb (Fig.

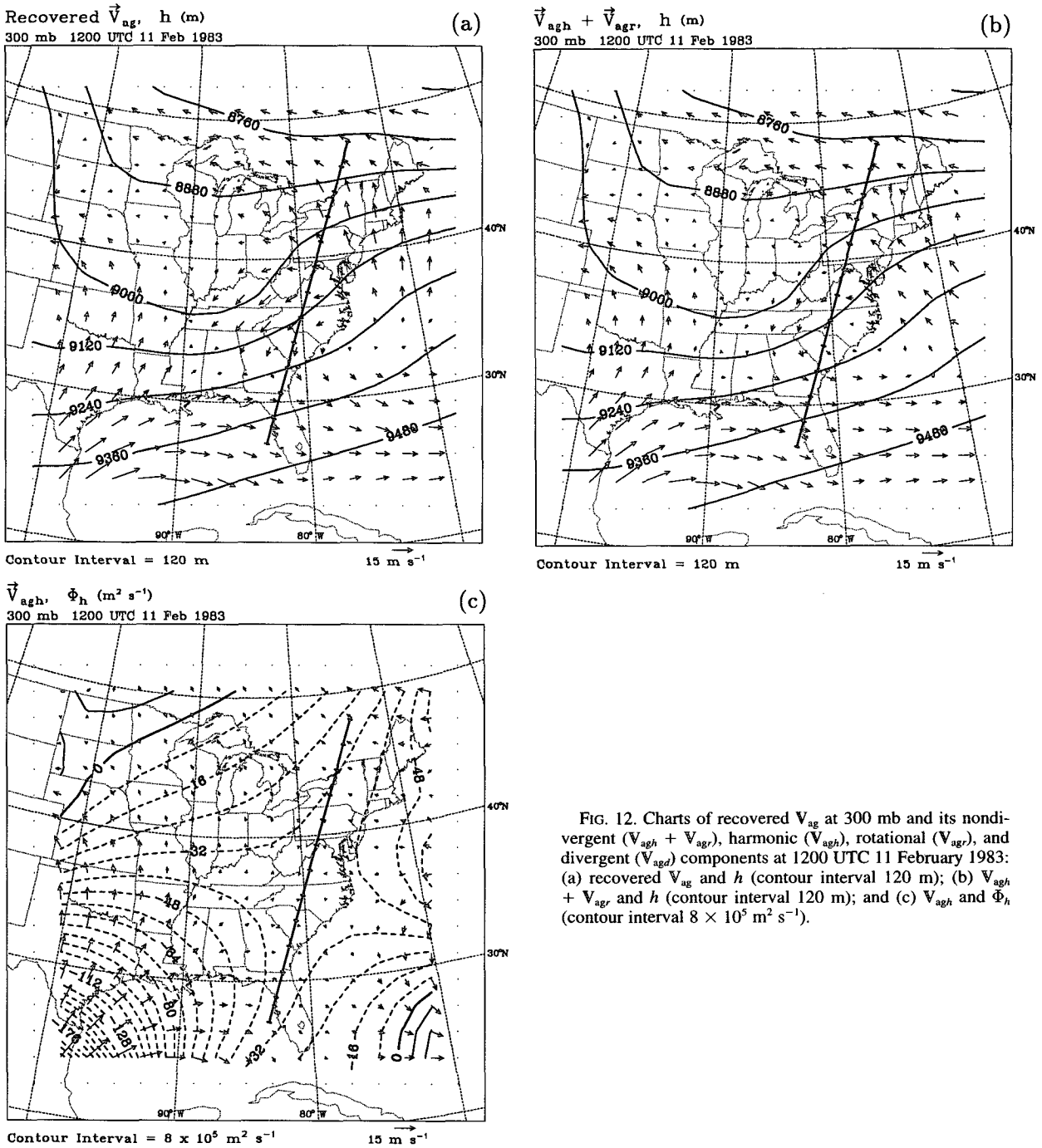

FIG. 12. Charts of recovered $\mathbf{V}_{ag}$ at 300 mb and its nondivergent ($\mathbf{V}_{agh} + \mathbf{V}_{agr}$), harmonic ($\mathbf{V}_{agh}$), rotational ($\mathbf{V}_{agr}$), and divergent ($\mathbf{V}_{agd}$) components at 1200 UTC 11 February 1983: (a) recovered $\mathbf{V}_{ag}$ and h (contour interval 120 m); (b) $\mathbf{V}_{agh} + \mathbf{V}_{agr}$ and h (contour interval 120 m); and (c) $\mathbf{V}_{agh}$ and Φ_h (contour interval 8×10^5 m^2 s^{-1}).

13b). The v_n pattern (Fig. 15a) resolves the northern and southern jet cores at 300 and 200 mb, respectively, as well as a low-level maximum associated with the easterly flow north of the cyclone. Figure 15b features a northward-sloping plume of high RH corresponding to the location of precipitation at the surface, along with an extensive region of small PV_e throughout the troposphere. The region of small tropospheric PV_e is shown in Fig. 15c to be associated with relatively small values of convective stability on the warm-air side of the deep baroclinic zone delineated by the θ_e field.

Three representations of transverse vertical circulations are illustrated in Fig. 16. The first of these, (v_s, ω) (Fig. 16a), reveals a region of deep slantwise ascent directed up the baroclinic zone in the θ_e field, consistent with the orientation of the plume of high RH and the

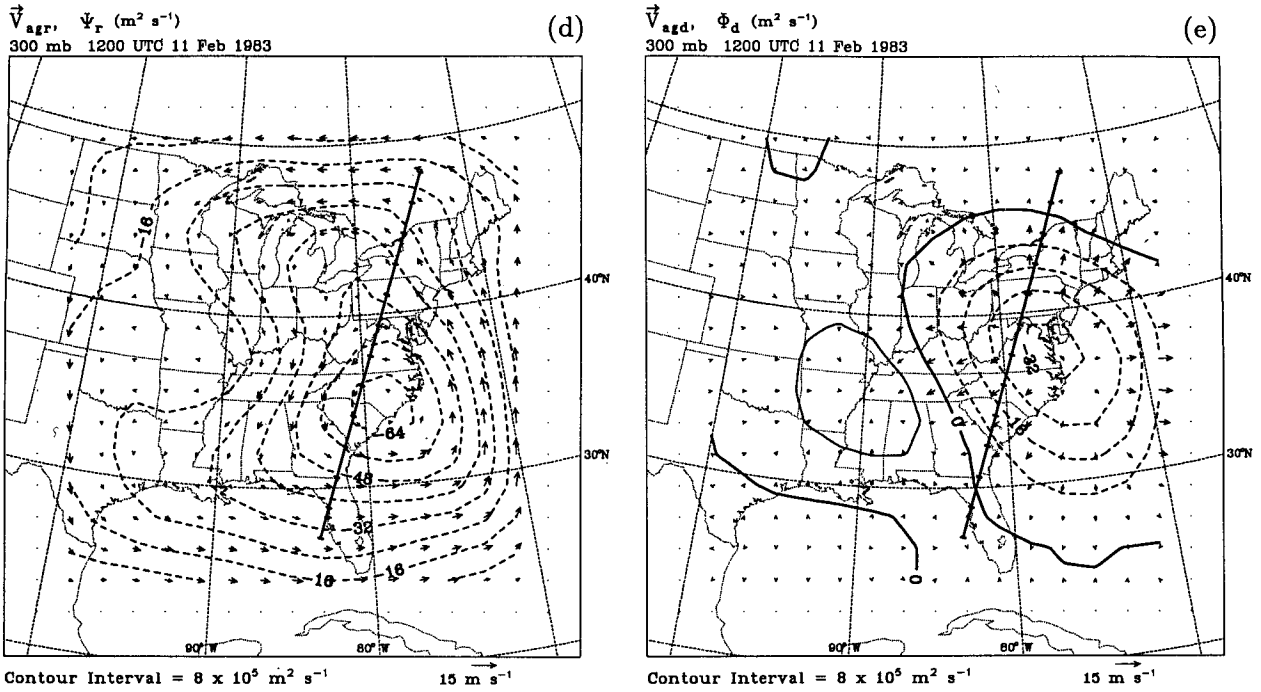

FIG. 12. (*Continued*) (d) $\mathbf{V}_{agr}$ and Ψ_r (contour interval 8×10^5 m^2 s^{-1}) and (e) $\mathbf{V}_{agd}$ and Φ_d (contour interval 8×10^5 m^2 s^{-1}).

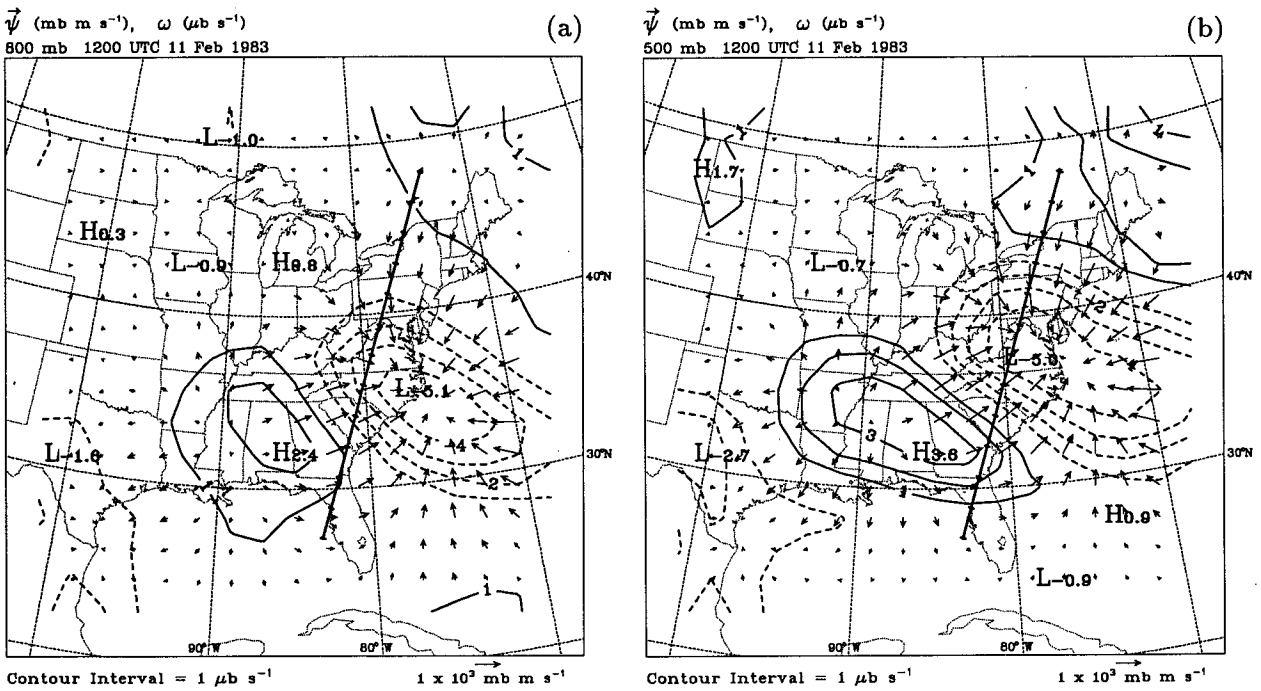

FIG. 13. Charts of ψ and kinematic ω (contour interval 1 μb s^{-1}, zero contours suppressed) at 1200 UTC 11 February 1983: (a) 800 mb; (b) 500 mb.

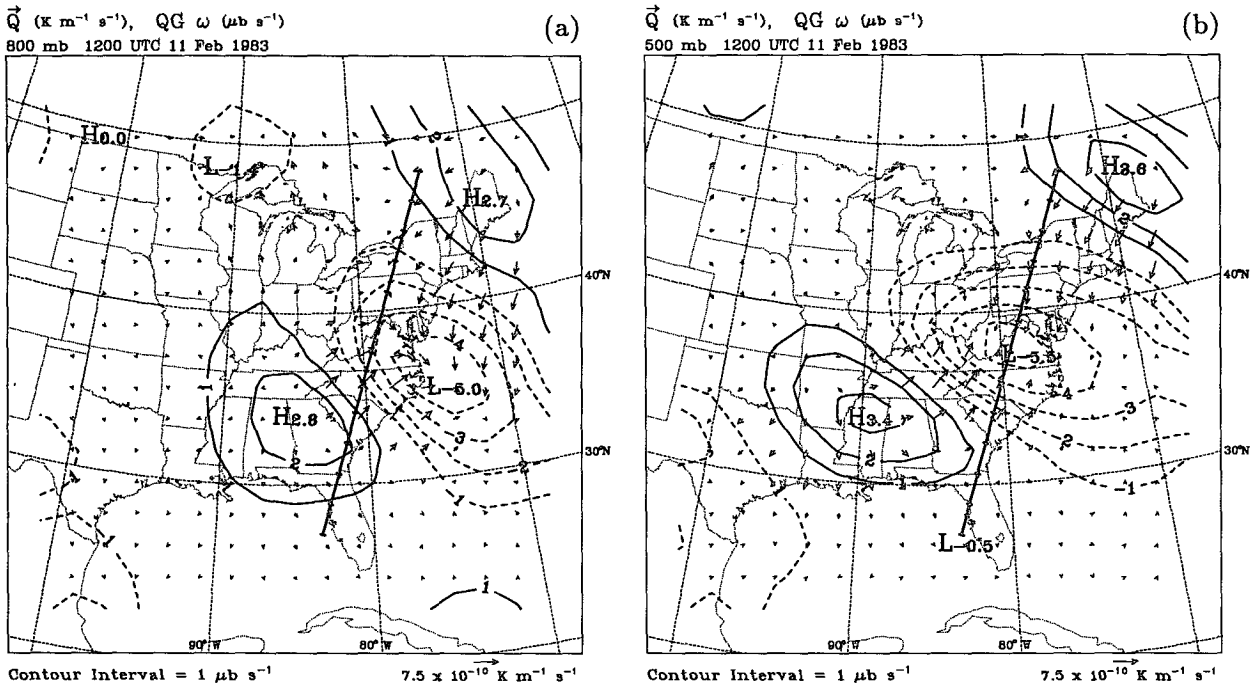

FIG. 14. Charts of Q and quasigeostrophic ω (contour interval 1 μb s^{-1}, zero contours suppressed) at 1200 UTC 11 February 1983: (a) 800 mb; (b) 500 mb.

distribution of precipitation (Figs. 15b,c). The second representation, (v_{ags}, ω) (Fig. 16b), indicates distinct direct and indirect vertical circulations corresponding to the northern and southern jets and in accord with expectations for jet entrance and exit regions, respectively. Similar signatures for the (v_{ags}, ω) representation are found in the cross sections for the M case presented by Emanuel (1985, Fig. 8) and UK (Fig. 8), although allowance needs to be made for differences in position between these respective cross sections and those of the present study.

The two-cell vertical circulation signature is reproduced by the (v_{agds}, ω_s) representation (Fig. 16c), which displays a well-defined band of northward-sloping ascent between the circulation cells. The qualitative agreement between Figs. 16b and 16c in this case is consistent with the noticeable contribution of $\mathbf{V}_{agd}$ to the cross-contour ageostrophic wind cited in the foregoing discussion of Fig. 12e. The northward-sloping updraft evident in the ψ_s field in Fig. 16c also is seen in the total ω field (Fig. 17a); comparison between ω_s (Fig. 17b) and ω_n (Fig. 17c) reveals that ω_s dominates ω_n by a factor of almost 2 to 1 in the updraft, and, as in the PD case, the spatial scale of the updraft in the ω_s field is smaller than that of the ω_n field. The dominance of ω_s is consistent with the orientation of the cross section and the geometry of the kinematic ascent maximum noted earlier in relation to Fig. 13b: scaling of the Laplacian operator (2.18), which defines the partition between ω_s and ω_n, reveals that $|\omega_s/\omega_n| \sim (L_n/L_s)^2$ (KSD, p. 2481), where L_s and L_n are characteristic length scales of the χ (and ω) fields tangential and normal to the selected orientation of the cross section. Inspection of Figs. 13a,b shows that L_s and L_n correspond closely to the minor and major axes of the elliptically shaped ascent region, confirming the dominance of ω_s relative to ω_n. The dominance of the tangential component of the divergent ageostrophic circulation in the present case lends quantitative support to UK's explanation of slantwise ascent in the inflection region between the axis of the upstream trough and the downstream confluence zone in terms of laterally coupled jet streak circulations.

5. Summary

We have adapted the kinematic methodology proposed by Keyser et al. (1989) for representing and diagnosing three-dimensional ageostrophic circulations into a form suitable for real-data applications involving limited-area domains. This adaptation incorporates the three-component partition of a two-dimensional vector field described by Lynch (1989) as applied to the ageostrophic wind. The geostrophic wind is defined in terms of constant Coriolis parameter so that it is nondivergent. This simplification allows the vertical velocity to be associated with the divergent part of the ageostrophic wind. A key aspect of the present methodology is the representation of the divergent part of the ageostrophic wind and the total vertical velocity in terms of

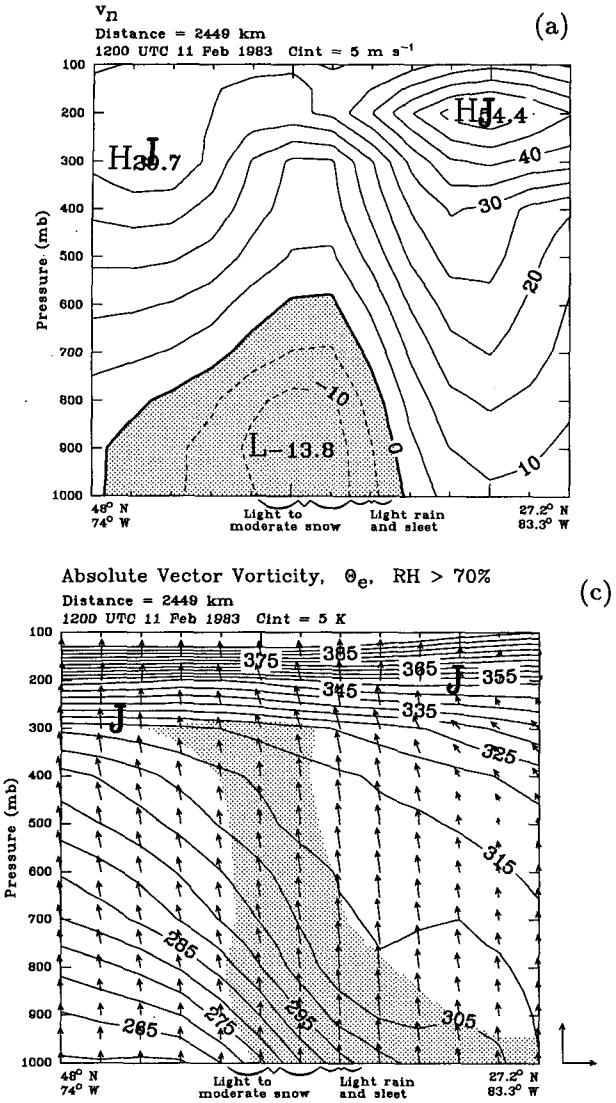

FIG. 15. Cross sections at 1200 UTC 11 February 1983 of (a) v_n (contour interval 5 m s^{-1}, negative values shaded); (b) PV_e (contour interval 0.5 PVU) and RH (values in excess of 70% shaded); (c) projection of ζ_a onto the cross-sectional plane, θ_e (contour interval 5 K), and RH (values in excess of 70% shaded). In these and subsequent cross sections shown at 1200 UTC 11 February 1983 (Figs. 16 and 17), latitude–longitude endpoints of the cross section, upper-level jets (J), and regions of precipitation are indicated. The distance between tick marks on the cross section abscissa is 200 km measured with respect to the grid; the total distance of 2449 km, indicated in the title block, is measured with respect to the earth. In (a), negative (positive) values denote flow out of (into) the page. In (c), the magnitudes of the vertical and horizontal scales of the reference vector are 27.16×10^{-5} s^{-1} and 54.31×10^{-5} m s^{-1} μb^{-1}, respectively.

a vector streamfunction (i.e., the psi vector), facilitating the directional partition of divergent ageostrophic circulations into components that may be projected onto arbitrarily oriented orthogonal vertical planes. This directional-partitioning property is argued to be especially useful for isolating divergent circulations in vertical planes tangential and normal to anisotropic flow features, such as (but not limited to) jet–front systems. Specifically, the partitioning is defined such that vertical circulations project increasingly onto the vertical plane transverse to jet–front systems as their associated vertical motion patterns become increasingly elongated in the alongfront direction. Thus, the psi-vector representation offers an objective means to assess quantitatively the two-dimensionality of divergent ageostrophic circulations and thus to test the validity and applicability of a variety of conceptual models of ageostrophic circulations in jet–front systems.

The present methodology is applied to two cases of well-documented cyclone events that occurred along the east coast of the United States at times in their respective evolutions where well-known conceptual models of ageostrophic circulations in upper-level jet–front systems can be examined: the Presidents' Day storm (at 1200 UTC 19 February 1979) and the Megalopolitan storm (at 1200 UTC 11 February 1983). In the Presidents' Day storm, the primary feature of interest is a cyclonically curved jet streak situated near the base of a short-wave trough; our analysis supports the interpretation that ascent in the southwesterly flow inflection, coinciding with the jet streak exit region, may be viewed as a superposition of vertical circulations associated with the jet–front system and with the baroclinic wave in which the jet–front system is embedded.

The foregoing interpretation views the total midtropospheric vertical motion field ω as consisting of a di-

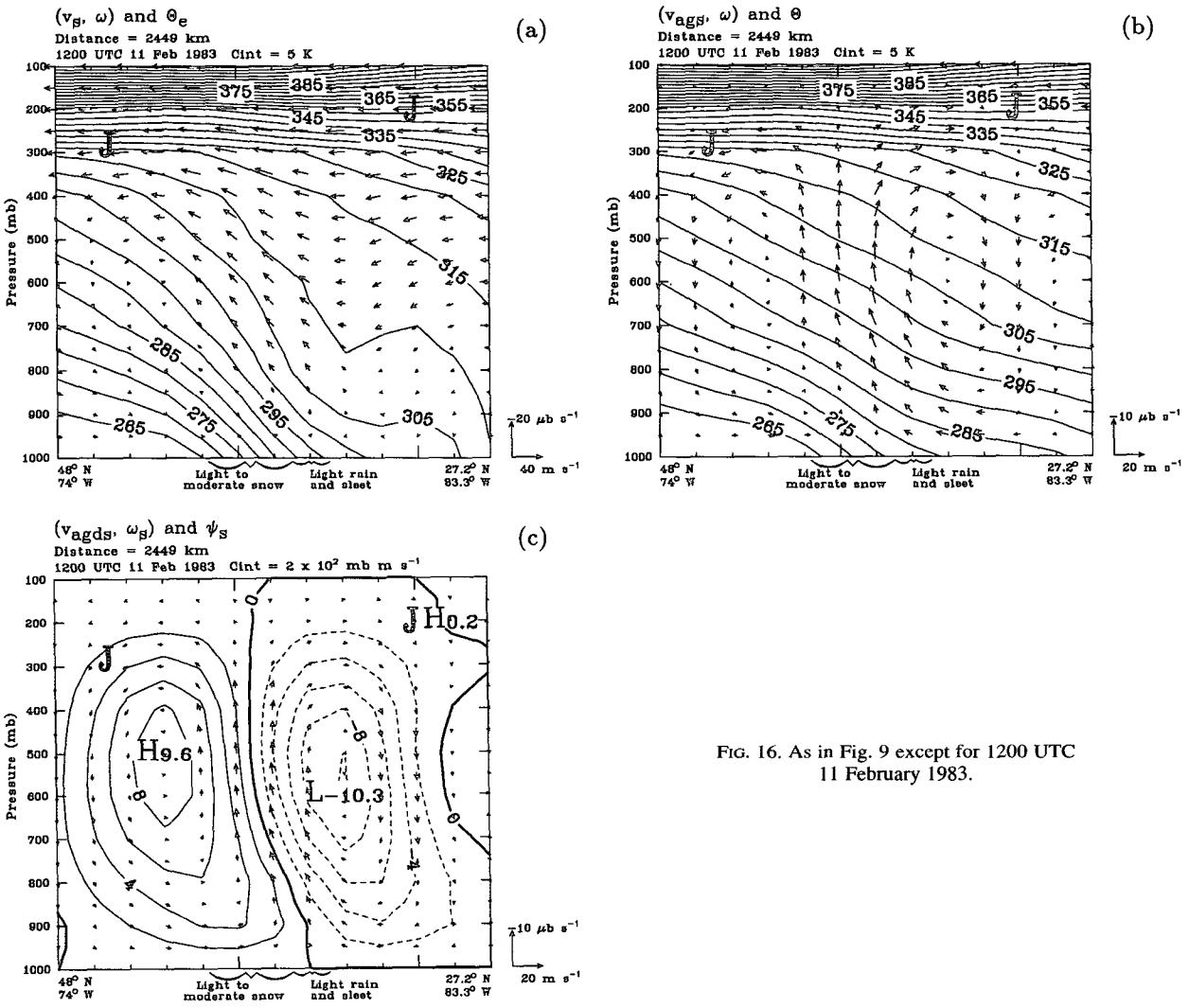

FIG. 16. As in Fig. 9 except for 1200 UTC 11 February 1983.

pole pattern composed of cells of descent and ascent elongated in the cross-stream direction, providing the "baroclinic-wave" component of the vertical circulation, upon which are superposed smaller-scale cells of descent and ascent elongated in the alongstream direction, providing the "jet streak" component of the vertical circulation. This interpretation, which is consistent with the kinematic ω pattern for the Presidents' Day case (Fig. 6), is demonstrated for a vertical cross section traversing the southwesterly flow inflection of the short-wave-trough–jet system located over the mid-Atlantic states. It is shown (Fig. 10) that the vertical motion component normal to the cross section consists of broad-scale ascent characteristic of the baroclinic wave, whereas the vertical motion component tangential to the cross section consists of a region of ascent exhibiting mesoscale detail. This detail takes the form of a dual updraft straddling the upper-level jet core, where the northern feature is hypothesized to be a manifestation of the updraft in the left exit region of a jet streak and the southern feature to be associated with a convective line.

In the Megalopolitan storm, we examine the conceptual model proposed by Uccellini and Kocin (1987) describing vertical circulations transverse to laterally displaced jet streaks: a northern jet streak embedded within a confluence zone downstream of a short-wave trough and a southern jet streak situated within the base of a short-wave trough. In this conceptualization, the midtropospheric ascent maximum in the southwesterly flow inflection of the short-wave trough is hypothesized to be the result of adjacent direct and indirect vertical circulations associated with the northern and southern jets, respectively. For a cross section oriented approximately normal to the jet entrance and exit regions, the cross-jet component of ascent dominates its along-jet counterpart by a factor of about 2 to 1, consistent with the orientation of the major axis of the elliptical ascent

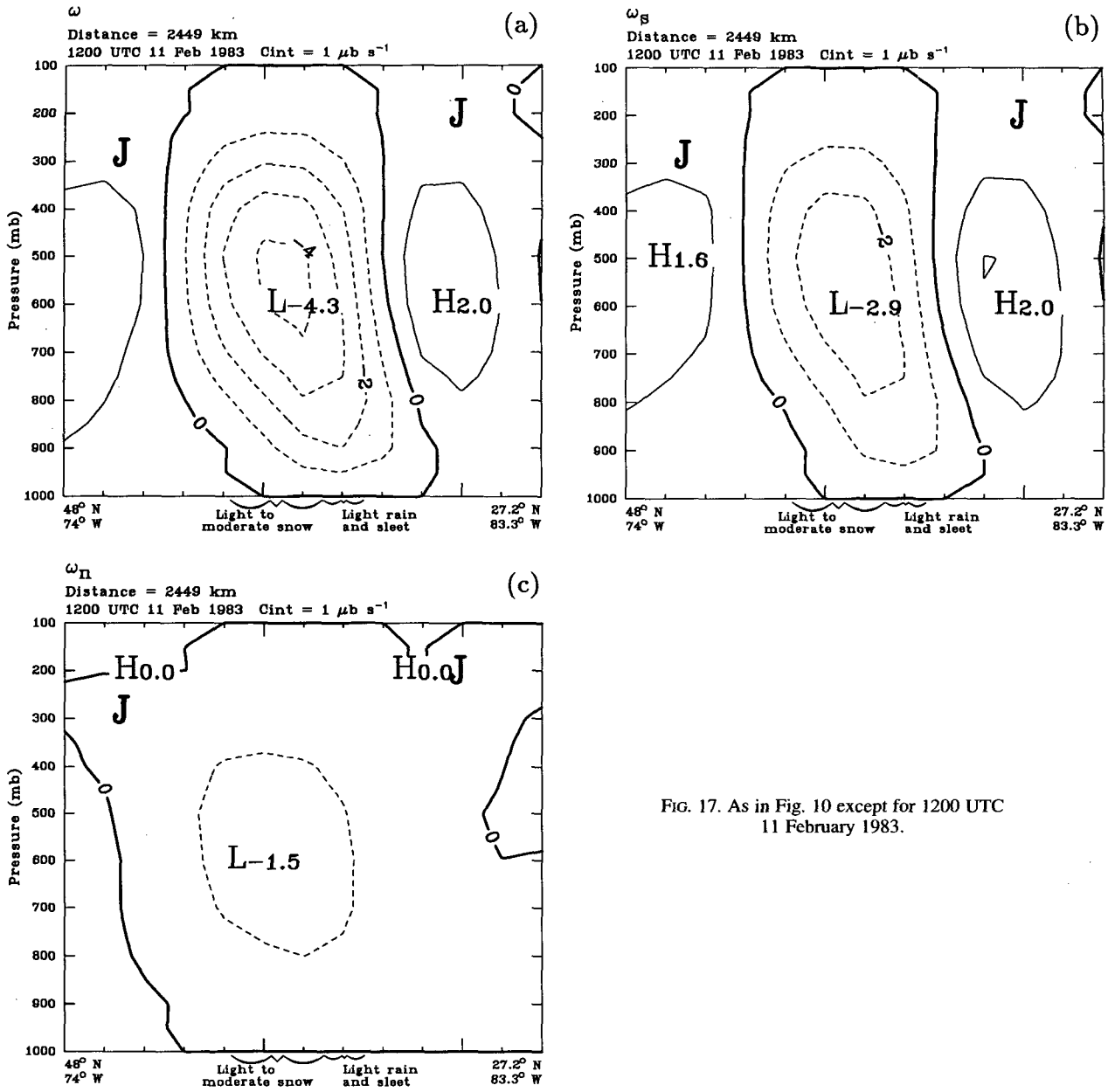

FIG. 17. As in Fig. 10 except for 1200 UTC 11 February 1983.

region approximately in the along-jet direction. The dominant contribution of ascent in the cross-jet vertical plane lends support to the explanation proposed by Uccellini and Kocin (1987) that slantwise ascent in the southwesterly flow inflection between the axis of the upstream trough and the downstream confluence zone is the result of laterally coupled jet streak circulations.

In both of the foregoing cases, application of the three-component partition of the ageostrophic wind supports the finding of Keyser et al. (1989), based on diagnosis of upper-level jet–front systems in an idealized channel-model simulation of the evolution of a baroclinic wave disturbance, that the ageostrophic wind is dominated by its nondivergent (i.e., harmonic plus rotational) part. This result provides additional support to the concern raised in Keyser et al. (1989) that the practice of linking cross-contour ageostrophic winds and vertical motions in jet entrance and exit regions in the qualitative assessment of energy transformations in these regions may be problematic for upper-level jet–front systems situated within three-dimensional flows. The basis for this concern is that the kinematic requirements satisfied by the cross-contour ageostrophic wind component in relation to Lagrangian rates of change of wind speed may be accomplished primarily by the nondivergent ageostrophic wind. This view does not imply

that the divergent ageostrophic wind cannot contribute to parcel accelerations in both wind speed and direction; examples are shown in both observational cases of augmentation of cross- and alongflow nondivergent ageostrophic winds by the divergent part of the ageostrophic wind. It is suggested that because vertical motions are kinematically independent of the nondivergent ageostrophic wind they should be considered only in relation to the divergent ageostrophic wind in diagnoses of upper-level jet–front systems situated in three-dimensional flows.

There are several limitations to the psi-vector methodology as applied to the present study. The first is the neglect of terrain, which, in principle, requires reformulation of the technique to account for a height-dependent lower boundary and specification of nonzero vertical motion at this boundary. The potential complexity of incorporating terrain effects suggests consideration of sigma coordinates, which allow the lower boundary to be maintained as a coordinate surface, as well as preservation of the condition of vanishing vertical motion. A likely disadvantage is that in regions of sloping terrain the physical interpretation of the three-way partition of the ageostrophic wind is no longer the same as in pressure coordinates, nor is the geostrophic wind nondivergent. A second limitation is the domain dependence of the three-component partition of the ageostrophic wind. As datasets and computing power permit, the domain-dependence problem may be solved by adopting global geometry, which eliminates the harmonic component from consideration.

A third limitation of the psi-vector approach is its kinematic basis; its design restricts it to directional partitioning based on the geometrical configuration of vertical motion patterns. Thus, it is not possible to perform dynamical attribution of ageostrophic circulations to discrete flow features—such as jets, fronts, waves, and vortices—through piecewise partitioning of the total flow, as is possible, for example, using quasigeostrophic potential vorticity inversion, provided that features of interest can be isolated through judicious combinations of interior potential vorticity and boundary conditions (e.g., Holopainen and Kaurola 1991; Davis 1992; Hakim et al. 1994). Another possibility is termwise partitioning of the vertical motion (or vertical circulation) among forcing terms that capture desired aspects of flow features, such as the separation of the Q vector into components normal and tangential to isentropes (Keyser et al. 1988, 1992b; Kurz 1992) to isolate quadripole and dipole vertical motion patterns related to jet streak and short-wave features, respectively (Barnes and Colman 1993, 1994). Similarly, consideration of the QG divergence equation [e.g., Eq. (3.6) of Xu (1990); Eq. (2.4) of Xu (1992)] allows the ageostrophic vorticity, and thus the rotational part of the ageostrophic wind, to be separated into contributions proportional to the square of the resultant geostrophic deformation and minus the square of the geostrophic relative vorticity. This result appears to be consistent with the presence of the anticyclonic gyre in the rotational ageostrophic flow within the upper-level short-wave trough in the Presidents' Day case (Fig. 5d), corresponding to a region of relatively large cyclonic geostrophic vorticity, and the cyclonic gyre in the region between the two upper-level jet streaks in the Megalopolitan storm case (Fig. 12d), where the influence of geostrophic deformation may be expected to be significant. Finally, the dynamical counterpart of the psi-vector methodology appropriate to channel-model geometry, as proposed and illustrated by Keyser et al. (1992a), may be modified to apply to limited-area domain geometry on conformal map projections in order to address the question of dynamical attribution through termwise partitioning.

Acknowledgments. We thank Dr. R. A. Anthes for making available his notes on conformal map projections, Dr. L. F. Bosart for providing us with the gridded dataset for the Presidents' Day storm documented in Bosart and Lin (1984), T. P.-J. Lee for advice in obtaining the dataset for the Megalopolitan storm, and M. Peacock for assisting in the preparation of the figures. We appreciate the comments and suggestions offered by Drs. S. L. Barnes, C. H. Bishop, R. L. Elsberry, J. C. Jusem, and two anonymous reviewers, which allowed us to refine the presentation of this research. Financial support of this research was provided by the National Science Foundation through NSF Grants ATM-8721478 and ATM-9114743 and by the Office of Naval Research through ONR Contract N00014-88-K-0074 and ONR Grant N00014-92-J-1532, awarded to the State University of New York at Albany.

REFERENCES

Anthes, R. A., E.-Y. Hsie, and Y.-H. Kuo, 1987: Description of the Penn State/NCAR mesoscale model version 4 (MM4). NCAR Tech. Note NCAR/TN-282+STR, 66 pp.

Barnes, S. L., and B. R. Colman, 1993: Quasigeostrophic diagnosis of cyclogenesis associated with a cutoff extratropical cyclone—The Christmas 1987 storm. *Mon. Wea. Rev.*, **121**, 1613–1634.

——, and ——, 1994: Diagnosing an operational numerical model using Q-vector and potential vorticity concepts. *Wea. Forecasting*, **9**, 85–102.

Beebe, R. G., and F. C. Bates, 1955: A mechanism for assisting in the release of convective instability. *Mon. Wea. Rev.*, **83**, 1–10.

Bennetts, D. A., and B. J. Hoskins, 1979: Conditional symmetric instability—A possible explanation for frontal rainbands. *Quart. J. Roy. Meteor. Soc.*, **105**, 945–962.

Bijlsma, S. J., L. M. Hafkenscheid, and P. Lynch, 1986: Computation of the streamfunction and velocity potential and reconstruction of the wind field. *Mon. Wea. Rev.*, **114**, 1547–1551.

Bishop, C. H., 1995: Domain independent attribution. Part I: Reconstructing the wind from G4 estimates of vorticity and divergence using free space Green's functions. *J. Atmos. Sci.*, **52**, submitted.

Blackburn, M., 1985: Interpretation of ageostrophic winds and implications for jet stream maintenance. *J. Atmos. Sci.*, **42**, 2604–2620.

Bolton, D., 1980: The computation of equivalent potential temperature. *Mon. Wea. Rev.*, **108**, 1046–1053.

Bosart, L. F., 1981: The Presidents' Day snowstorm of 18–19 February 1979: A subsynoptic-scale event. *Mon. Wea. Rev.*, **109**, 1542–1566.

——, and S. C. Lin, 1984: A diagnostic analysis of the Presidents' Day snowstorm of February 1979. *Mon. Wea. Rev.*, **112,** 2148–2177.

Chen, Q.-S., and Y.-H. Kuo, 1992a: A harmonic-sine series expansion and its application to partitioning and reconstruction problems in a limited area. *Mon. Wea. Rev.*, **120,** 91–112.

——, and ——, 1992b: A consistency condition for wind-field reconstruction in a limited area and a harmonic-cosine series expansion. *Mon. Wea. Rev.*, **120,** 2653–2670.

Danard, M., 1989: On computing viscous forces in map coordinates with a variable scale. *Mon. Wea. Rev.*, **117,** 2829–2834.

Davis, C. A., 1992: Piecewise potential vorticity inversion. *J. Atmos. Sci.*, **49,** 1397–1411.

Dutton, J. A., 1986: *The Ceaseless Wind: An Introduction to the Theory of Atmospheric Motion.* Dover, 617 pp.

Eliassen, A., 1984: Geostrophy. *Quart. J. Roy. Meteor. Soc.*, **110,** 1–12.

——, 1990: Transverse circulations in frontal zones. *Extratropical Cyclones,* The Erik Palmén Memorial Volume, C. W. Newton and E. O. Holopainen, Eds., Amer. Meteor. Soc., 155–165.

Emanuel, K. A., 1983a: The Lagrangian parcel dynamics of moist symmetric instability. *J. Atmos. Sci.*, **40,** 2368–2376.

——, 1983b: On assessing local conditional symmetric instability from atmospheric soundings. *Mon. Wea. Rev.*, **111,** 2016–2033.

——, 1985: Frontal circulations in the presence of small moist symmetric stability. *J. Atmos. Sci.*, **42,** 1062–1071.

——, 1994: *Atmospheric Convection.* Oxford University Press, 580 pp.

Hakim, G. J., and L. W. Uccellini, 1992: Diagnosing coupled jet-streak circulations for a northern plains snow band from the operational nested-grid model. *Wea. Forecasting,* **7,** 26–48.

——, D. Keyser, and L. F. Bosart, 1994: Diagnosis of wave–merger cyclogenesis through quasi-geostrophic potential vorticity inversion. *Proc. Int. Symp. on the Life Cycles of Extratropical Cyclones,* Vol. II, S. Grønås and M. A. Shapiro, Eds., Geophysical Institute, University of Bergen, Norway, 221–226.

Haltiner, G. J., and R. T. Williams, 1980: *Numerical Prediction and Dynamic Meteorology.* 2nd ed. Wiley, 477 pp.

Holopainen, E., and J. Kaurola, 1991: Decomposing the atmospheric flow using potential vorticity framework. *J. Atmos. Sci.*, **48,** 2614–2625.

Holton, J. R., 1992: *An Introduction to Dynamic Meteorology.* 3rd ed. Int. Geophys. Ser., Vol. 48, Academic Press, 511 pp.

Hoskins, B. J., 1975: The geostrophic momentum approximation and the semi-geostrophic equations. *J. Atmos. Sci.*, **32,** 233–242.

——, 1982: The mathematical theory of frontogenesis. *Annu. Rev. Fluid Mech.*, **14,** 131–151.

——, and I. Draghici, 1977: The forcing of ageostrophic motion according to the semi-geostrophic equations and in an isentropic coordinate model. *J. Atmos. Sci.*, **34,** 1859–1867.

——, and M. A. Pedder, 1980: The diagnosis of middle latitude synoptic development. *Quart. J. Roy. Meteor. Soc.*, **106,** 707–719.

——, I. Draghici, and H. C. Davies, 1978: A new look at the ω-equation. *Quart. J. Roy. Meteor. Soc.*, **104,** 31–38.

Keyser, D., 1994: On the representation and diagnosis of frontal circulations in two and three dimensions. *Proc. Int. Symp. on the Life Cycles of Extratropical Cyclones,* Vol. I, S. Grønås and M. A. Shapiro, Eds., Geophysical Institute, University of Bergen, Norway, 193–207.

——, and M. A. Shapiro, 1986: A review of the structure and dynamics of upper-level frontal zones. *Mon. Wea. Rev.*, **114,** 452–499.

——, M. J. Reeder, and R. J. Reed, 1988: A generalization of Petterssen's frontogenesis function and its relation to the forcing of vertical motion. *Mon. Wea. Rev.*, **116,** 762–780.

——, B. D. Schmidt, and D. G. Duffy, 1989: A technique for representing three-dimensional vertical circulations in baroclinic disturbances. *Mon. Wea. Rev.*, **117,** 2463–2494.

——, ——, and ——, 1992a: Quasigeostrophic diagnosis of three-dimensional ageostrophic circulations in an idealized baroclinic disturbance. *Mon. Wea. Rev.*, **120,** 698–730.

——, ——, and ——, 1992b: Quasigeostrophic vertical motions diagnosed from along- and cross-isentrope components of the **Q** vector. *Mon. Wea. Rev.*, **120,** 731–741.

Knight, D. J., and P. V. Hobbs, 1988: The mesoscale and microscale structure and organization of clouds and precipitation in midlatitude cyclones. Part XV: A numerical modeling study of frontogenesis and cold-frontal rainbands. *J. Atmos. Sci.*, **45,** 915–930.

Kocin, P. J., and L. W. Uccellini, 1990: *Snowstorms along the Northeastern Coast of the United States: 1955 to 1985. Meteor. Monogr.*, No. 44, Amer. Meteor. Soc., 280 pp.

Krishnamurti, T. N., 1968: A study of a developing wave cyclone. *Mon. Wea. Rev.*, **96,** 208–217.

Kurz, M., 1992: Synoptic diagnosis of frontogenetic and cyclogenetic processes. *Meteor. Atmos. Phys.*, **48,** 77–91.

Loughe, A. F., 1992: Real-data diagnosis of partitioned ageostrophic vertical circulations. M.S. thesis, State University of New York at Albany, 138 pp. [Available from Department of Atmospheric Science, State University of New York at Albany, ES-219, Albany, NY 12222.]

Lynch, P., 1988: Deducing the wind from vorticity and divergence. *Mon. Wea. Rev.*, **116,** 86–93.

——, 1989: Partitioning the wind in a limited domain. *Mon. Wea. Rev.*, **117,** 1492–1500.

Moore, J. T., and G. E. VanKnowe, 1992: The effect of jet-streak curvature on kinematic fields. *Mon. Wea. Rev.*, **120,** 2429–2441.

O'Brien, J. J., 1970: Alternative solutions to the classical vertical velocity problem. *J. Appl. Meteor.*, **9,** 197–203.

Sanders, F., and L. F. Bosart, 1985: Mesoscale structure in the Megalopolitan snowstorm of 11–12 February 1983. Part I: Frontogenetical forcing and symmetric instability. *J. Atmos. Sci.*, **42,** 1050–1061.

Sangster, W. E., 1960: A method of representing the horizontal pressure force without reduction of station pressures to sea level. *J. Meteor.*, **17,** 166–176.

Saucier, W. J., 1955: *Principles of Meteorological Analysis.* University of Chicago Press, 438 pp.

Shapiro, M. A., and P. J. Kennedy, 1981: Research aircraft measurements of jet stream geostrophic and ageostrophic winds. *J. Atmos. Sci.*, **38,** 2642–2652.

Uccellini, L. W., 1990: Processes contributing to the rapid development of extratropical cyclones. *Extratropical Cyclones,* The Erik Palmén Memorial Volume, C. W. Newton and E. O. Holopainen, Eds., Amer. Meteor. Soc., 81–105.

——, and P. J. Kocin, 1987: The interaction of jet streak circulations during heavy snow events along the east coast of the United States. *Wea. Forecasting,* **1,** 289–308.

——, P. J. Kocin, R. A. Petersen, C. H. Wash, and K. F. Brill, 1984: The Presidents' Day cyclone of 18–19 February 1979: Synoptic overview and analysis of the subtropical jet streak influencing the pre-cyclogenetic period. *Mon. Wea. Rev.*, **112,** 31–55.

——, D. Keyser, K. F. Brill, and C. H. Wash, 1985: The Presidents' Day cyclone of 18–19 February 1979: Influence of upstream trough amplification and associated tropopause folding on rapid cyclogenesis. *Mon. Wea. Rev.*, **113,** 962–988.

Xu, Q., 1990: Cold and warm frontal circulations in an idealized moist semigeostrophic baroclinic wave. *J. Atmos. Sci.*, **47,** 2337–2352.

——, 1992: Ageostrophic pseudovorticity and geostrophic C-vector forcing—A new look at the Q vector in three dimensions. *J. Atmos. Sci.*, **49,** 981–990.

——, and D. Keyser, 1993: Barotropic and baroclinic ageostrophic winds and completeness of solution for the psi equations. *J. Atmos. Sci.*, **50,** 588–596.